

Chapter 8

Colloidal Nanosheets

Nobuyoshi Miyamoto, Yutaka Ohsedo and Teruyuki Nakato

8.1 Introduction

Nanosheet materials are obtained as colloidal dispersions through the exfoliation of a layered solid in a solvent. In many cases, colloidal dispersions of nanosheets are considered homogeneous and structureless dispersions that are just a passing point for the fabrication of many types of important solid-state nanomaterials, as introduced in other chapters of this book.

However, we emphasize that the nanosheet colloids themselves have controllable meso-scale structures and intriguing properties and functions. From the viewpoint of fundamental colloid sciences, nanosheet colloids are regarded as a very unusual colloidal system compared to other ordinary colloids because of the huge anisotropy of the particles. From the viewpoint of practical applications, nanosheet colloids serve as functional soft materials due to their interesting rheological properties, liquid crystallinity, and response to external stimuli. In addition, we can expect the development of smart soft materials by coupling the properties of nanosheet colloids with various functions inherent to the inorganic nanosheets, such as their electric, catalytic, magnetic, and optical properties. To obtain functional solid-state nanomaterials using nanosheets as nanomodules, it is also important to understand and control the structure and properties of the nanosheets in the state of colloidal dispersion because most of these solid materials are fabricated using colloidal dispersions of nanosheets as a precursor.

N. Miyamoto (✉) · Y. Ohsedo

Department of Life, Environment, and Materials Science, Fukuoka Institute of Technology,
3-30-1 Wajiro-higashi, Higashi-ku, Fukuoka 811-0295, Japan
e-mail: miyamoto@fit.ac.jp

T. Nakato

Department of Applied Chemistry, Kyushu Institute of Technology, 1-1 Sensui-cho,
Tobata-ku, Kitakyushu-shi, Fukuoka 804-8550, Japan

© Springer Japan KK 2017

T. Nakato et al. (eds.), *Inorganic Nanosheets and Nanosheet-Based Materials*,
Nanostructure Science and Technology, DOI 10.1007/978-4-431-56496-6_8

This chapter addresses colloidal nanosheets dispersed in a solvent. Starting with the fundamental aspects of the nanosheet colloids based on classical models, we then focus on the two important aspects of the nanosheet colloids: liquid crystal phase formation and rheological properties. Theories related to the colloid properties are also described. The studies on applications of the nanosheet colloids for soft materials and nanofabrication are also introduced.

8.2 Classical Theory of Colloids Applicable for Nanosheets

Let us first start with a general description of the classical models of colloids: the Stern model and DLVO theory [1]. In these models, the surface charge is important because it determines the stability and structure formation of a colloidal dispersion. Generally, colloid particles are charged in water, regardless of their chemical composition. Even if the particle has an electrostatically neutral chemical composition, the particle is normally charged due to dissociation or protonation of the surface functional groups. In the case of a particle of an oxide MO_x , where M is Si, Al, Fe, etc., the charge depends on pH because the hydroxy groups on the particle dissociate into $\text{M}-\text{O}^-$ and H^+ at higher pH, while it is protonated to form positively charged $\text{M}-\text{OH}_2^+$ at lower pH. The charge becomes zero at intermediate pH, which is called the point of zero charge. The amount of charge on the surface is quantified by the charge density σ_0 [C m^{-2}] or surface potential ψ_0 [V]. However, these values are difficult to directly measure experimentally. Hence, the zeta potential ζ [V], which is the potential at the *slipping surface* of the particle, is generally used. The zeta potential is slightly lower than the surface potential.

The charge of the particles should be compensated by the same amount of opposite charge of the counter ions. The Stern model is the standard model to depict the spatial distribution of the counter ions around the particle. According to this model, the particle is surrounded by an electric double layer composed of a Stern layer and a Gouy–Chapman layer (or diffuse layer). The Stern layer is the first layer in which the ions are strongly bound onto the particle surface due to the affinity of the ions to the surface. In the Gouy–Chapman layer, the ions are weakly bound to the particle and form an *ionic cloud*. The concentration of counter ions, or potential, decreases as the distance x from the surface increases. Under some assumptions and approximations, the potential at distance x is expressed as

$$\psi = \psi_0 \exp(-\kappa x). \quad (8.1)$$

Here, κ^{-1} is called as Debye screening length, which is usually regarded as a measure of the thickness of the diffuse layer and is expressed as

$$\kappa^{-1} = \sqrt{\frac{\varepsilon_r \varepsilon_0 kT}{2000 N_A e^2 I}}, \quad (8.2)$$

where ε_r is the specific dielectric constant of the solvent, ε_0 is the dielectric constant of vacuum, T is temperature, k is Boltzmann's constant, N_A is the Avogadro's constant, e is the charge of an electron, and I is the ionic strength. An important point is that the thickness of the diffuse layer decreases with increasing ionic strength I .

The simplest theory on the interactions between colloid particles is the DLVO (Derjaguin–Landau–Verwey–Overbeek) theory [1]. In this theory, the potential energy V_T for a pair of colloid particles is expressed as the sum of van der Waals attraction V_A and the repulsion V_R due to overlap of the diffuse layers as

$$V_T = V_A + V_R. \quad (8.3)$$

The potential due to attraction between two parallel thin plates with thickness L , which are separated by distance h , is expressed as

$$V_A = -\frac{A}{12\pi} \left\{ \frac{1}{h^2} + \frac{1}{(h+2L)^2} - \frac{2}{(h+L)^2} \right\}, \quad (8.4)$$

$$\sim \frac{A}{2\pi} \frac{L^2}{h^4} \text{ (if } L \ll h \text{)}$$

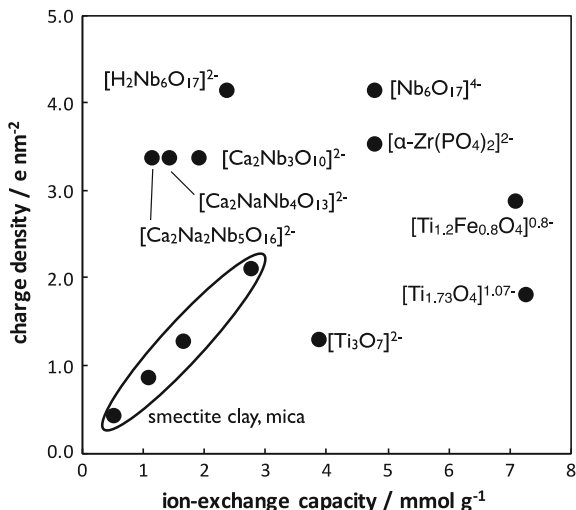
where A is the Hamaker constant, which indicates the strength of the van der Waals interaction. The repulsion term is expressed as

$$V_R = \frac{64nkT}{\kappa} \left[\tanh\left(\frac{e\psi_0}{4kT}\right) \right] \exp(-\kappa h). \quad (8.5)$$

Based on DLVO theory, we can discuss the stability of the dispersed state and the structure formation of a colloid. When the ionic strength is lower and the surface charge is higher, the repulsion V_R is dominant, giving a maximum on the V_T – h curve. In this case, the colloid dispersion is stable and the average distance between the particles is determined simply based on the particle concentration. When the ionic strength is higher and the surface charge is lower, the attraction force V_A dominates the system so that V_T is always negative and only the deep minimum appears on the curve. In this case, the colloid particles aggregate. With intermediate ionic strength and surface charge, a shallow, secondary minimum sometimes appears on the V_T – h curve as a result of the balancing of V_R and V_A . In this case, the particles may be loosely trapped at the position of the secondary minimum. These behaviors are qualitatively in accordance with many experiments, as shown in Chap. 3, while quantitative formulation is difficult with this simple theory.

To apply these theories to nanosheet colloids, Eqs. (8.1)–(8.5) can be valid, but the charge of the nanosheets should be considered. Most known nanosheets, such as

Fig. 8.1 Comparison of the charge densities of nanosheets



clay minerals, metal oxides, metal phosphates, and graphene oxides, are negatively charged, while the rare example is layered double hydroxides that have permanent positive charges. The ideal charge density for each layered material can be calculated based on the chemical composition and crystal structure. Comparison by the unit of [$e \text{ nm}^{-2}$], charge per unit surface area, is useful for many purposes, while, in the case of clay minerals, the unit of [meq g^{-1}] is often used. Figure 8.1 compares the ideal layer charge of several nanosheet materials. The charge density ranges from 0.5 to 4.0 [$e \text{ nm}^{-2}$], and the ion exchange capacity ranges from 0.5 to 8 [meq g^{-1}]. For a nanosheet surface with this range of layer charge, a surface potential as high as several hundreds of mV is expected. However, a zeta potential value of several tens of mV is often obtained experimentally [2] due to a low dissociation constant of the surface group and adsorption of counter ions in the Stern layer, which is largely affected by the type of counter cations. In contrast to most other materials, smectite-type clay minerals have permanent negative charges inside the layer, while the edge charge depends on the pH due to the presence of hydroxy group. The edges are normally negatively charged at higher pH, at which we usually address clay colloids. We note there are many publications in which the discussions are based on the misunderstanding that the edge is always positively charged.

8.3 Liquid Crystal Phases of Nanosheet Colloids

Because of the huge anisotropy of nanosheets, the nanosheet colloids form liquid crystal (LC) phases. In a dilute colloidal dispersion, nanosheets are moving around in translational and rotational manners, that is, Brownian motion. However, if the

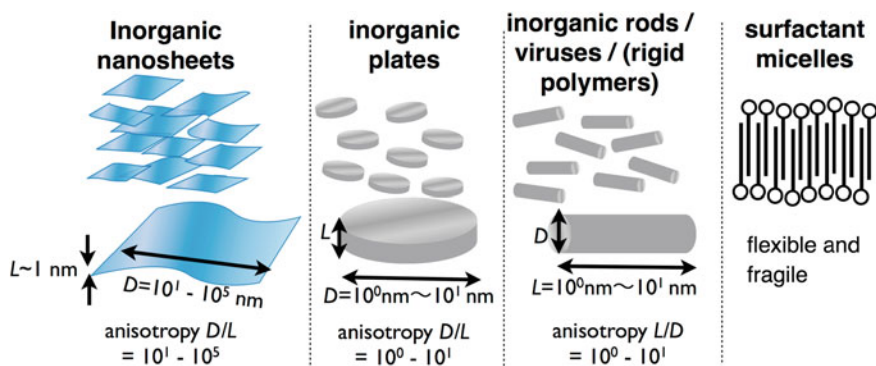


Fig. 8.2 Comparison of lyotropic liquid crystals based on nanosheets, plates, rods, and surfactants

concentration of the nanosheets increases, the free rotational motion is restricted and the nanosheets cooperatively orient themselves along a certain direction to form an LC phase. We have named this type of liquid crystals as *nanosheet liquid crystals* and have been studying these materials as a new type inorganic LCs. Nanosheet LCs are classified as a lyotropic LCs, as distinguished from thermotropic LCs. A lyotropic LC is generally composed of a solvent and anisotropic dispersoids, and the LC phase formation depends on the concentration of the dispersoid. Many types of lyotropic LCs have been reported, as shown in Fig. 8.2: surfactant micelles, rigid polymers [3–5] (e.g., poly(paraphenylene terephthalamide) and DNA), rod-shaped particles (viruses [6], metals [7], oxides [8–10], and semiconductors [11]), nanoplates (gibbsite ($\text{Al}(\text{OH})_3$) [12, 13], $\text{Ni}(\text{OH})_2$ [14], and layered double hydroxides [15]), and nanosheets. Among them, nanosheets are regarded as ultimately anisotropic two-dimensional particles.

Although many nanosheet materials have been reported so far, only a few of them are reported as nanosheet liquid crystals for several reasons. One reason is that, in some cases, only a lower degree of exfoliation and lower yield of exfoliated single-layered nanosheets can be attained. In other cases, the colloids themselves are unstable so that they precipitate and aggregate within short time, preventing their use as a colloidal material. It is also a problem that, as often observed in layered clay mineral systems, the colloidal dispersions becomes viscose or gelled at low concentration, and the characterization as a fluid liquid crystal cannot be performed. Considering various applications, it is desirable that the system has a wider concentration range for the liquid crystal phase with high fluidity. Therefore, it is important to optimize various parameters, such as particle size, distribution of the particle size, and salt concentration, to improve the properties of the colloid to be suitable for nanosheet liquid crystal materials. Although we have a few numbers of the examples satisfying these conditions, Figs. 8.3 and 8.4 summarize the schematic structures of the reported nanosheet LCs and the phase diagram, respectively. In the following subsections, the individual research works of each material will be presented.

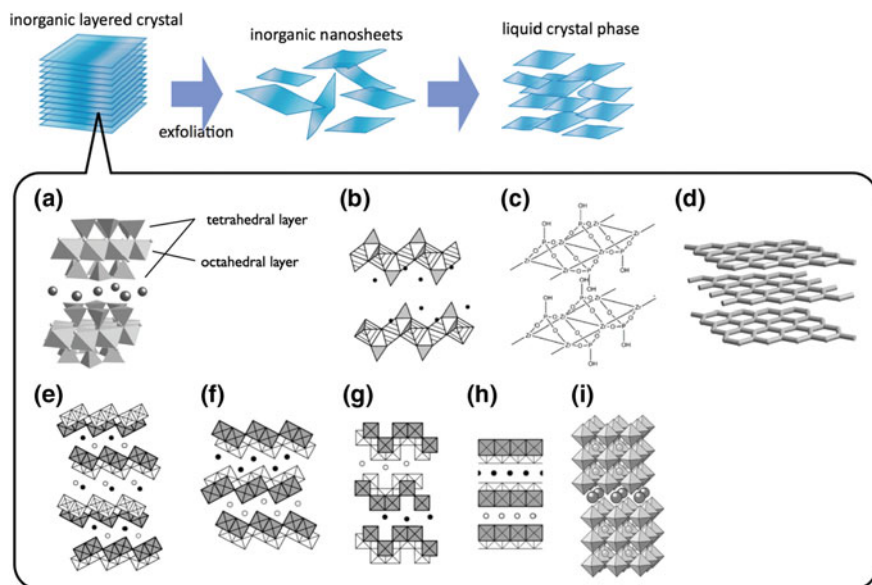


Fig. 8.3 Schematic model of intercalation, exfoliation, and liquid crystal phase formation, and the structures of the layered materials that form liquid crystal phases: **a** clay mineral, **b** $K_3Sb_3P_2O_{14}$, **c** α -ZrP, **d** graphite, and transition metal oxides of **e** $K_4Nb_6O_{17}$, **f** $KTiNbO_5$, **g** KNb_3O_8 , **h** $Cs_{1.07}Ti_{1.73}O_4$ and **i** $KCaNb_3O_{10}$

8.3.1 Layered Phosphates

In a 2001 article in *Nature* [16], Gabriel et al. reported phosphoric antimony nanosheets obtained from layered $K_2Sb_3P_2O_{14}$ as a nanosheet LC with a swollen lamellar structure. $K_2Sb_3P_2O_{14}$ is composed of SbO_6 octahedrons and PO_4 tetrahedrons combined with a shared apex (Fig. 8.3b). The layer has a thickness of 1.1 nm, and the negative charges are compensated by interlayer K^+ . The homogeneous, clear, and transparent nanosheet colloid was obtained by exchanging the interlayer K^+ with H^+ , followed by washing and dialysis. In contrast to most other systems, this material does not require the addition of a stabilizer or exfoliating agent. Figure 8.5 shows the phase diagram of this system. In the range of the nanosheet concentration of 0.75–1.78 vol.%, this colloid possesses fluidity and birefringence. At more than 1.78 vol.%, it becomes a gel with birefringence. Below 0.75 vol.%, it enters a biphasic state, that is, the coexistence of birefringent and isotropic phases. After storing the biphasic sample, the dense birefringent phase and the dilute isotropic phase are macroscopically separated into the lower and upper parts of the sample, respectively, with a clear interface. Because the isotropic phase shows flow-induced birefringence, this upper phase is confirmed to be a colloid with dispersed nanosheets but not a simple solvent. Although not mentioned in the literature, at lower concentration, the system should transition to a purely isotropic phase.

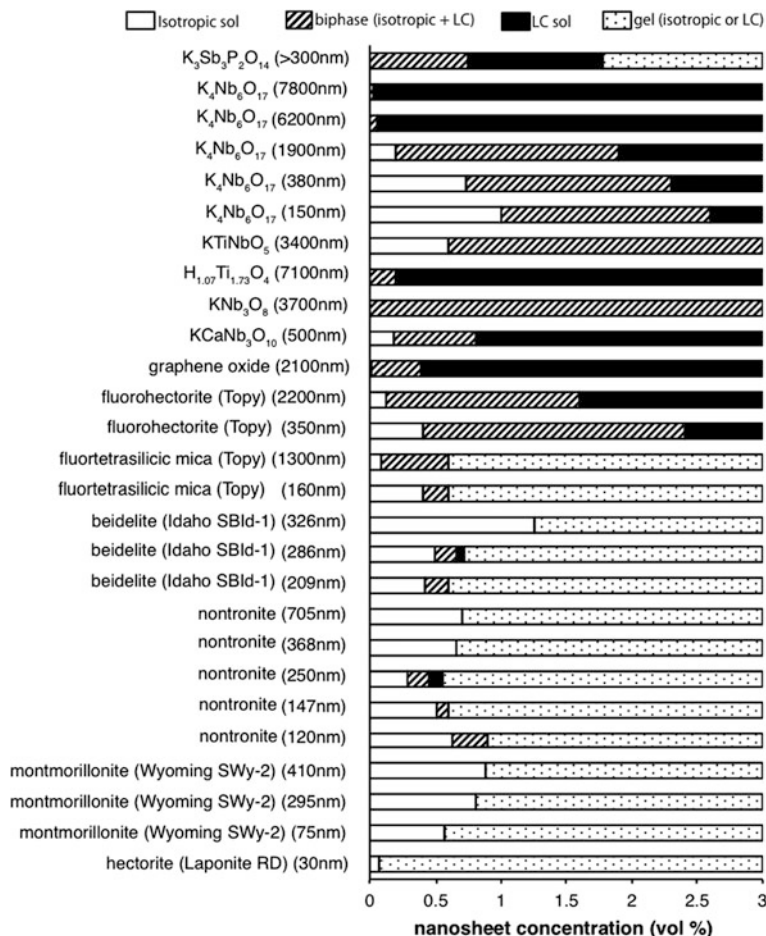
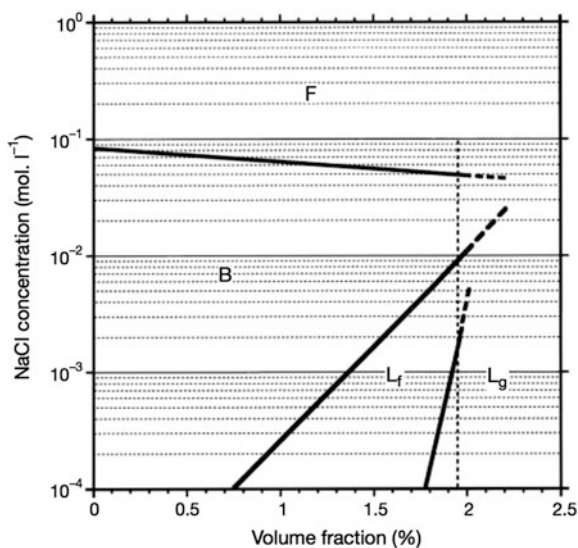


Fig. 8.4 The summary of the phase diagram of the aqueous nanosheet dispersions of $K_3Sb_3P_2O_{14}$ [16], $K_4Nb_6O_{17}$ [17], $KTiNbO_5$ [18], $H_{1.07}Ti_{1.73}O_4$ [19], KNb_3O_8 [18], $KCaNb_3O_{10}$ [20], graphene oxide [21], fluorohectorite [22], fluortetrasilic mica [22], beidelite [23], nontronite [24], montmorillonite [25], and hectorite [26] at relatively low salt concentrations, collected from the references. The *parenthetic values* are average lateral length of the nanosheets

Thus, with increasing concentration, the system transitions from the isotropic phase to the complete liquid crystal phase, passing through the coexistence of the two phases. This is the general behavior of anisotropic colloids as theoretically predicted by Onsager [27], the theory of which is explained in detail in Sect. 4.1.

In this system, a swollen lamellar structure with the basal spacing of up to 225 nm was identified by small-angle X-ray scattering (SAXS). As shown in Fig. 8.6a, multiple narrow diffraction peaks appeared, indicating high structural order. Because of the large basal spacing, structural colors from blue to red were observed under white illumination. Of the several reported nanosheet colloid

Fig. 8.5 Phase diagram of $\text{H}_3\text{Sb}_3\text{P}_2\text{O}_{14}$ suspensions versus volume fraction and salt concentration. Upon decreasing the volume fraction, the suspensions first form a lamellar gel phase (L_g), then a lamellar fluid phase (L_f) and finally enter a biphasic regime (B). The system flocculates (F) at high salt molarity. Reprinted with permission from Ref. [16]. Copyright 2001 Nature Publishing Group



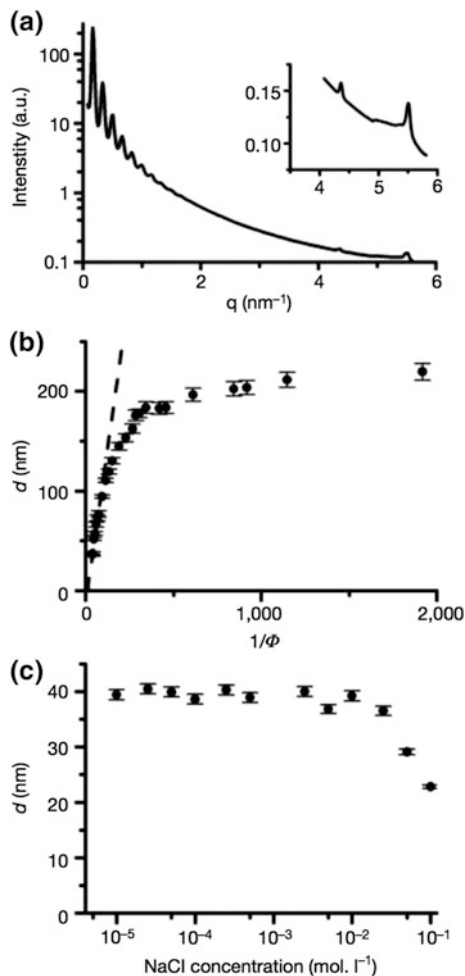
systems, there are only a few examples with the very large basal spacing, high structural order, and structural colors observed in this system. As shown in Fig. 8.6b, the basal spacing d increases with decreasing nanosheet concentration; it reaches the maximum of 225 nm. If the lamellar structure with layer thickness L undergoes ideal one-dimensional swelling, the basal spacing d follows the following formula,

$$d = L/\varphi^{-1}. \quad (8.6)$$

In the range of $\varphi^{-1} < 100$, the plot in Fig. 8.6b follows this formula. Extrapolation of the straight line gives the value $L = 1.05$ nm, and this value approximately coincides with the crystallographically estimated thickness of the nanosheet. By adding the salt to the colloid, phenomena such as flocculation, gelation, and decrease of basal spacing (Fig. 8.6c) occurred. However, these phenomena occurred only when a salt concentration was more than 10^{-2} M. Thus, adding a small amount of salt does not greatly influence the state of the system.

As another phosphate nanosheet system, Cheng et al. investigated nanosheet colloids derived from layered zirconium phosphate α -ZrP [28]. In this report, powders of layered crystals of α -ZrP were synthesized by a hydrothermal method so that the average particle size and size distribution were precisely controlled by varying the reaction time and the concentration of the starting solution. Through exfoliation of these crystals, a series of the samples with different lateral size and size distribution were obtained. The phase transition concentrations ϕ_I (for the isotropic phase to biphasic) and ϕ_N (for the biphasic to liquid crystal phase) for these samples are shown in Fig. 8.7. Both ϕ_I and ϕ_N decrease with increasing average particle size. Although Miyamoto et al. had already reported the influence of particle size at the time [17], the importance of Cheng's study is that they clarified

Fig. 8.6 Small-angle X-ray scattering (SAXS) study of the liquid crystalline antimonophosphate nanosheet colloid. **a** The SAXS pattern of the sample of 2.0 vol. %. **b** Variation of the basal spacing d with the inverse of the concentration. **c** Variation of the basal spacing d with the NaCl concentration added to the system of $\phi = 1.9$ vol. %. Reprinted with permission from Ref. [16]. Copyright 2001 Nature Publishing Group



the effect of the particle size distribution. As the particle size distribution increased, ϕ_N exceedingly increased, while ϕ_I did not change, resulting in widening of the concentration range for the biphasic and the coexistence of the isotropic and LC phases. This result is in harmony with the theoretical prediction by the modified Onsager's theory. Moreover, Cheng et al. reported the α -ZrP system, of which the nanosheet surface is chemically modified with thermosensitive poly(*N*-isopropylacrylamide). This system showed reversible liquid crystal-isotropic phase transition induced by temperature change.

Recently, by adsorbing the amphiphilic polyoxyalkyleneamine onto the surface of α -ZrP nanosheets, Wong et al. [29] prepared nanosheets dispersed in nonaqueous solvent, butyronitrile, stabilized by the steric effect of the adsorbed polymer layer. Nanosheet LCs dispersed in organic solvent are applicable for the fabrication of

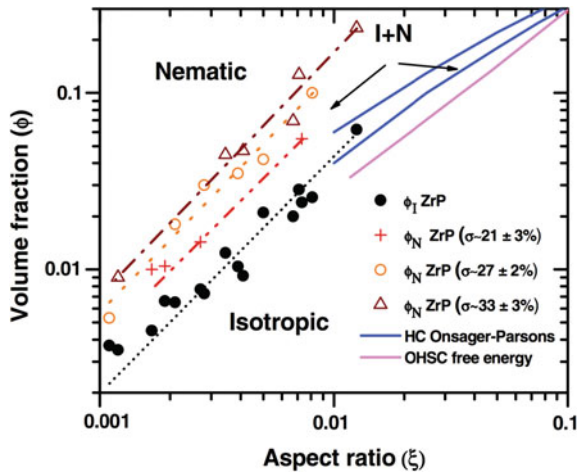


Fig. 8.7 Comparison of the experimental ϕ_I and ϕ_N with those evaluated by the Monte Carlo simulation based on the free energy calculation with oblate hard spherocylinders (OHSC) model, and the Onsager-Parsons theory based on hard cylinder (HC) models. The power law scaling of 2 for ϕ are (filled circle) $\phi_I = 23.1 \pm 8.12^{1.36 \pm 0.10}$, (open triangle) $\phi_N = 115.5 \pm 78.62^{1.41 \pm 0.20}$, (open circle) $\phi_N = 68.6 \pm 48.32^{1.36 \pm 0.10}$ and (plus) $\phi_N = 36.9 \pm 6.92^{1.32 \pm 0.04}$. The lines are guides for the eye. Reprinted with permission from Ref. [28]. Copyright 2012 American Physical Society

various inorganic/organic composites, although such a system has not been reported previously. Furthermore, in this system, similarly to the study of $K_3Sb_3P_2O_{14}$ reported by Gabriel [16], a lamellar structure with very large basal spacing of up to ca. 240 nm was confirmed, and structural colors attributable to this structure were observed (Fig. 8.8).

8.3.2 Layered Transition Metal Oxides

In 2002, Miyamoto and Nakato reported a liquid crystal nanosheet colloid prepared from the layered niobate, $K_4Nb_6O_{17}$ [30, 31]. They also confirmed the liquid crystallinity in the related oxide materials, such as $KTiNbO_5$ [18], KNb_3O_8 [18], and $H_{1.07}Ti_{1.73}O_4$ [19]. In 2004, they clarified the effect of the lateral size of the nanosheets on the formation of the LC phase for the first time. In that study, nanosheets with controlled large lateral size were obtained by exfoliation of a $K_4Nb_6O_{17}$ crystal of cm scale, synthesized by the flux method [32]. The obtained colloid was ultrasonicated to crush the nanosheets to a smaller average size, as controlled by the duration of the ultrasonication. A series of samples with average particle size ranging from 0.15 to 7.8 μm were obtained. The dependence of ϕ_I and ϕ_N on the average lateral size of the nanosheets is summarized in Table 8.1.

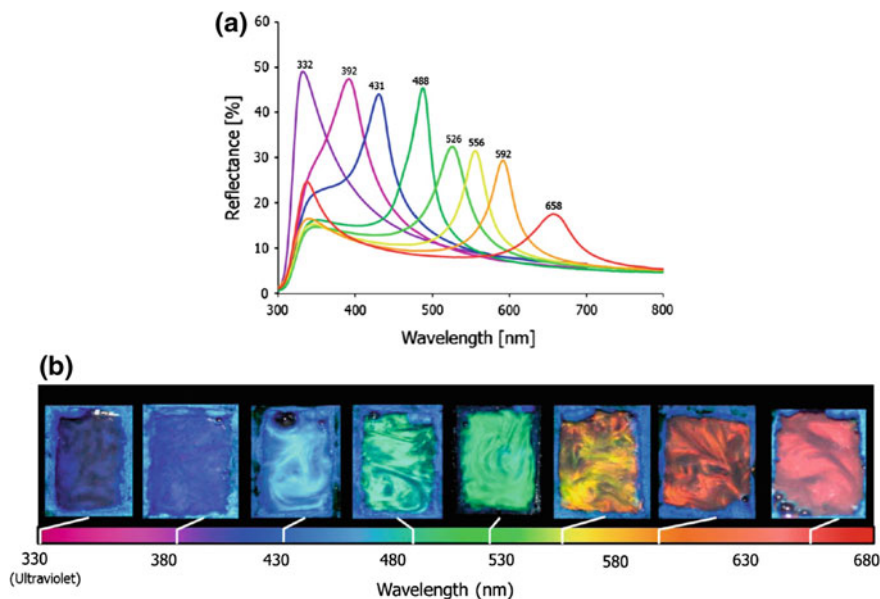


Fig. 8.8 Photonic crystals of nanoplatelets in organic solution. **a** Reflection spectra of 625 nm α -ZrP nanoplatelets in butyronitrile at various concentrations. Reflectance peak shifts from red to ultraviolet as concentration of nanoplatelets increases. **b** Photographic images of butyronitrile solutions containing α -ZrP nanoplatelets demonstrating colors shifting from violet to red as concentration decreases from left to right. Reprinted with permission from Ref. [29]. Copyright 2014 American Chemical Society

Table 8.1 Mean lateral sizes and critical concentrations of the phase transitions

Ultrasonication/min	$D_m/\mu\text{m}$	$\sigma_{(\log)}$	$\phi_1^a(\text{vol/vol})$	$\phi_{LC}^b(\text{vol/vol})$
0	7.8	9.2	$<5 \times 10^{-2}$	$\sim 3 \times 10^{-3}$
10	6.2	7.7	$<5 \times 10^{-2}$	$\sim 5 \times 10^{-3}$
50	1.9	6.8	1.9×10^{-3}	1.9×10^{-2}
90	0.38	9.5	7.3×10^{-3}	2.3×10^{-2}
180	0.15	11	1.0×10^{-2}	2.6×10^{-2}
0 (from powder)	3.6	9.8		

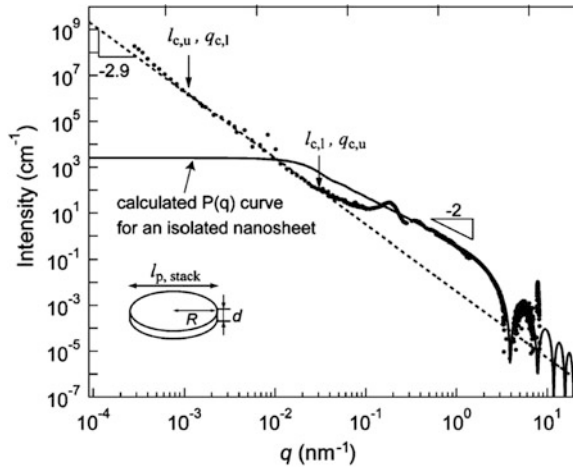
Reprinted with permission from Ref. [17]. Copyright 2004 American Chemical Society

^aThe concentration where the colloid transits from isotropic to biphasic

^bThe concentration where the colloid transits from biphasic to liquid crystalline

The simple trend is found that ϕ_1 increases as the average particle size increases. This trend roughly coincides with the prediction of Onsager theory. This niobate system is advantageous because the fluidic liquid crystal phase is obtained in a very large concentration range. Owing to the fluidity, macroscopic orientation by an

Fig. 8.9 Analysis of the scattering profile of an aqueous dispersion of niobate nanosheets. Reprinted with permission from Ref. [34]. Copyright 2007 International Union of Crystallography



external field is easy. The liquid crystal phase of the niobate nanosheets with an adsorbed organic dye was macroscopically aligned by gravitational field, providing a hierarchical organization of the dye structure.

Yamaguchi et al. conducted detailed structural analyses for the $K_4Nb_6O_{17}$ nanosheet LC system [33, 34]. Figure 8.9 shows the combined small-angle neutron/X-ray scattering patterns for the nanosheets with an average particle size of 3200 nm. The scattering profile roughly coincides with the theoretical form factor $P(q)$ of a thin disc with radius R and thickness L . $P(q)$ is represented as follows:

$$P(q) = \left(\frac{2}{q^2 R^2} \right) \left[1 - \frac{J_1(2qR)}{qR} \right] \frac{\sin^2(qL/2)}{(qL/2)^2} \quad (8.7)$$

Here, q is the scattering vector and J_1 is the first-order Bessel function. This form factor is reduced as: $P(q) \sim q^{-2}$ in the range of $L^{-1} < q < R^{-1}$, $P(q) \sim 1$ in the range of $q < R^{-1}$, and $P(q) \sim q^{-4}$ in the range of $q > L^{-1}$. The solid line in Fig. 8.9 is the theoretical curve of $P(q)$ calculated with sufficiently large R and with $L = 1.6$ nm. Because the theoretical curve coincides well with the experimental results at $q > 10^0$, it is confirmed that there are mostly completely exfoliated nanosheets with the thickness of 1.6 nm in this colloid, rather than incompletely exfoliated layered crystals. In the range of $10^{-1} < q < 100$, several peaks appeared at the positions corresponding to $q/2\pi = 1/d, 2/d, 3/d$ and so on. The peaks are ascribed to the regulated structure with the basal spacing d . This suggests that there exists not only the orientational order explained by Onsager theory but also positional order in the nanosheet colloid forming the LC phase. In the ultra-small-angle region ($q < 10^{-2} \text{ nm}^{-1}$), the scattering of $q^{-2.9}$ is observed. This scattering is in excess compared to the q^{-2} expected for a two-dimensional object and may be ascribable to a fractal structure, which is composed of sparse and dense domains due to the inhomogeneous distribution of the nanosheets in the solvent. Several

studies have suggested the existence of fractal structures in nanosheet colloids [35–40]. The sparse and dense structure is formed because the system is not dominated by repulsive force; attractive interaction among the nanosheets also exists.

On the other hand, Miyamoto et al. [20] reported the LC phase of the nanosheet colloid obtained from $\text{KCa}_2\text{Nb}_3\text{O}_{10}$ (Fig. 8.3i). $\text{KCa}_2\text{Nb}_3\text{O}_{10}$ is a type of Dion–Jacobson layered perovskite with the general formula $\text{M}[\text{A}_{n-1}\text{B}_n\text{O}_{3n+1}]$ ($\text{M} = \text{K}, \text{Na}, \text{H}, \text{etc.}; \text{A} = \text{Ca}, \text{Ba}, \text{K}, \text{Sr}, \text{etc.}; \text{B} = \text{Nb}, \text{Ti}, \text{etc.}$) [41]. Layered perovskites are suitable for systematic basic research because a series of compounds with various chemical compositions and structures can be synthesized. In addition, the layered perovskites have intriguing functions, such as photocatalytic activity [42], catalytic activity as solid acids [43], and luminescent properties [44], so they are expected to be applicable to advanced soft materials.

8.3.3 Layered Clay Minerals

Layered clay minerals have been studied historically for the longest time of all layered materials and are very important materials for many types of industrial applications because of their low cost, abundance in earth soils, and low toxicity. The liquid crystallinity of a clay mineral was first reported by Langmuir in 1938 [45]. Langmuir found that the colloidal sol of bentonite clay produced in California had a birefringent texture, and he identified this as a liquid crystal phase. However, this observation was not reproduced and the liquid crystallinity of the clay mineral colloid was not reported for a long time afterward. One of the reasons is that most clay mineral colloids lose the fluidity at relatively low concentrations (at several wt %) and become physical gels. In many cases, the transition to a physical gel occurs below the concentration of the liquid crystal phase transition so that it is impossible to observe the emergence of the liquid crystal phase clearly. Even if birefringence is observed in the gel, it is difficult to confirm the permanent birefringence due to the liquid crystal phase, which should be distinguished by flow birefringence with very slow relaxation. In the late 1990, several research groups reported birefringent clay colloidal gels. In 1996, Gabriel et al. [46] carefully observed the gels of montmorillonite or hectorite and obtained birefringent gels at specific clay and salt concentrations. Mourchid et al. reported that hectorite formed a nematic liquid crystal phase at above 3 wt% [26]. Fossum et al. reported that the colloid of synthetic fluorohectorite was separated into three phases, the precipitate, birefringent gel, and isotropic, after allowing the colloid to stand for a period of time [47]. On the other hand, Michot et al. [25] reported that the montmorillonite colloid becomes a sol, gel, aggregate, or the partially birefringent gel depending on the particle size and salt concentration. However, the fluidity is lost in the nanosheet colloids in these reports, and it is difficult to confirm that these observations correspond to a true liquid crystal phase.

A clay mineral colloid with permanent birefringence and fluidity was reported by Michot et al. [24, 48, 49] in 2006 for the first time. The exfoliated nontronite

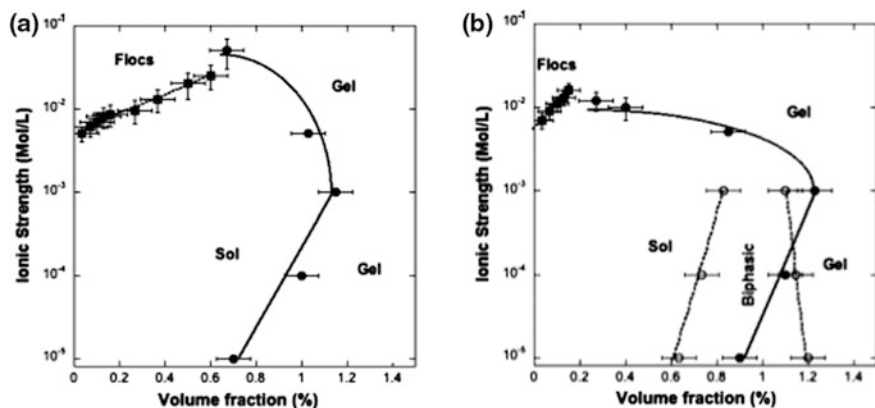
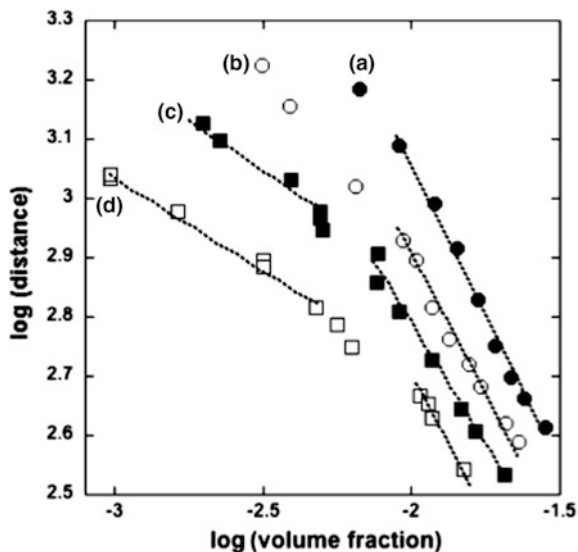


Fig. 8.10 Phase diagram of nontronite with an average lateral size of **a** 2200 nm and **b** 250 nm. Reprinted with permission from Ref. [24]. Copyright 2008 American Chemical Society

Fig. 8.11 Evolution of the average interparticular distances as functions of the concentration and average lateral size of the nanosheets at ionic strength of 10^{-5} M. The average size are *a* 2200, *b* 986, *c* 346 and *d* 250 nm, respectively. Reprinted with permission from Ref. [24]. Copyright 2008 American Chemical Society



nanosheet had a strip-like shape with a long side to short side ratio of 2.9–5.5, and the length of the long side was 2200 nm. Figure 8.10 shows the phase diagram with the particle size and ionic strength as the parameters. In the sample with small particle size (250 or 345 nm) and salt concentration less than 10^{-3} M, the phase transition from the isotropic phase to the liquid crystal phase occurred at a nanosheet concentration of 0.6–0.7 wt%. In contrast, in the sample with large average particle size, only the sol-gel transition was observed. In the relationship between the average particle-particle distance d determined by SAXS and the nanosheet concentration (Fig. 8.11), the system followed the law of one-dimensional swelling of

Eq. (8.6) in the region of high nanosheet concentration. On the other hand, d was proportional to $\phi^{1/3}$ in the range of the lower nanosheet concentration, which corresponds to isotropic swelling. Whereas the ionic strength did not greatly influence the liquid crystal phase transition, very high ionic strength caused flocculation or gelation.

Michot et al. also reported the liquid crystal formation of the natural beidellite clay system [23, 50]. Using several clay mineral systems, they conducted an investigation of the rheological, osmotic pressure, and SAXS measurements. Based on these observations, they concluded that the electrostatic repulsive force between nanosheets dominates the rheological properties and liquid crystallinity, while the hydrodynamic capture effect may also be related [50–52].

On the other hand, Miyamoto et al. [22] reported that the synthetic fluorohectorite and fluorotetrasilicic mica with controlled particle size prepared by purification and sonication processes formed liquid crystal phases with very high fluidity. Figure 8.12 shows photos of these colloids under crossed polarizers. The sample with large particle size has a texture with interference colors ascribable to the liquid crystal phase at 1.0 wt%, while typical phase separation behavior occurs (Fig. 8.12d–g). In contrast, the sample with small particle size at 1.0 wt% is isotropic and only shows flow birefringence (Fig. 8.12b, i), and the permanent liquid crystal phase (Fig. 8.8c, j) is observed only at the higher concentration (2.0 wt%).

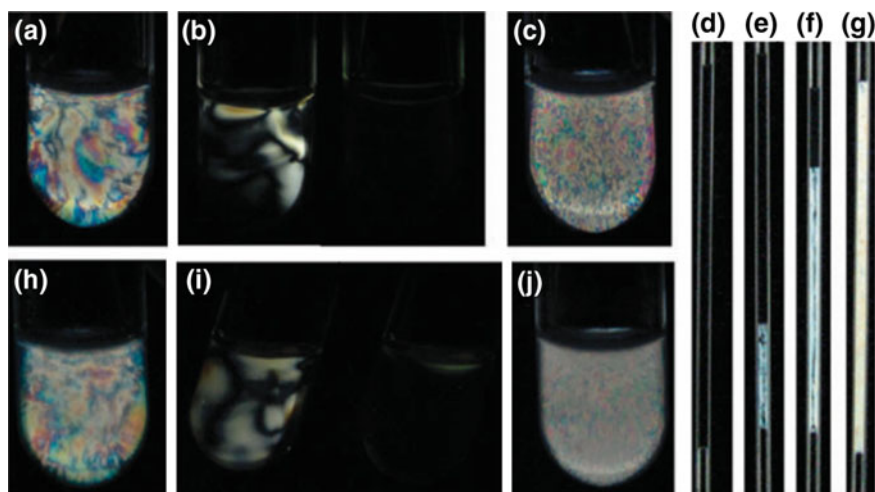


Fig. 8.12 Observation of the **a–g** FHT and **h–j** FTSM colloids in glass tubes (10 mm or 1 mm in diameter) with crossed polarizers: the mean lateral size $D =$ (**a**)(**d**)–(**g**) 2.2, (**b**)(**c**) 0.35, (**h**) 1.3, and (**i**)(**j**) 0.16 nm and the colloid concentration $c =$ (**a**)(**b**)(**h**)(**i**) 1.0, (**c**)(**j**) 2.0, (**d**) 0.28, (**e**) 0.81, (**f**) 2.0, (**g**) 4.0 wt%. The *left-hand* images of (**b**) and (**i**) are transient states observed just after shaking the tubes; they relax to a dark isotropic state (*right-hand* images) in a second. The photos (**a**)–(**c**) and (**h**)–(**j**) were taken just after preparation, while (**d**)–(**g**) were taken after macroscopic phase separation of the samples to upper isotropic and lower LC phases by standing the sample for 5 h. Reprinted with permission from Ref. [22]. Copyright 2010 The Royal Society of Chemistry

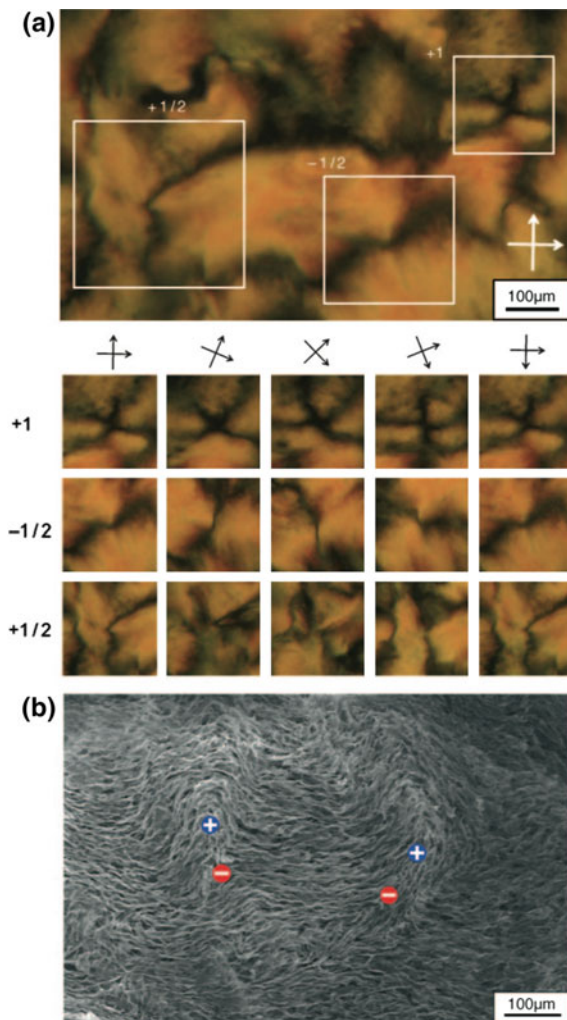
Compared to other clay mineral systems, these systems are very fluid up to very high concentrations, which is suitable for various basic research and applications. In these systems, gelation did not occur even at 7.0 wt%. Fossum et al. also investigated synthetic fluorohectorite systems; they used a sample with impurities. The viscosity was high, and it was difficult to study the phase behavior [47, 53]. In addition to these fluorinated clays, Miyamoto et al. found that the natural montmorillonite produced in Tsukinuno and purified by a similar method showed liquid crystallinity.

8.3.4 Graphene and Grapheme Oxide

Graphene has received much attention due to its excellent electronic and mechanical properties, and it was selected as the subject for the Nobel Prize in 2010. However, it is difficult to obtain a large amount of completely exfoliated graphene, and the graphene reported in many papers is not a nanosheet but a “stacked graphene”. There are few reports on the liquid crystal phase of graphene; Dan et al. [54] obtained exfoliated graphene with high yield by dispersing in chlorosulfonic acid and observed the schlieren texture, which is characteristic of nematic liquid crystals.

In contrast to graphenes, it is easy to obtain single-layer graphene *oxide* nanosheets dispersed in a solvent, and many investigations have been carried out. However, graphene oxides have hydroxyl and/or carboxyl groups irregularly placed on their surface, and they have no defined chemical structure. The electronic properties characteristic of graphene are not retained in the graphene oxides, but the lost electronic properties can be recovered to some extent by post-reduction treatments. The liquid crystal phase of a graphene oxide was reported in 2001, followed by many additional reports. Kim et al. [55] obtained a single graphene oxide nanosheet with the thickness of 0.8 nm and the average particle size ranging from 0.75 to 1.65 μm . They observed an optical texture characteristic of a nematic phase by polarized optical microscopy, and the structure was confirmed for the freeze-dried sample by SEM (Fig. 8.13). In the system with the particle size of 0.75 μm , the phase transition concentration was 0.78 wt%. Aboutalebi et al. [56] prepared graphene oxide with the much larger average particle size of 33 μm , and the system had the ϕ_1 of 0.1 wt%. Xu et al. [21] investigated the graphene oxide with the average particle size of 2.1 μm . This system had the ϕ_1 of 0.025 wt% and the ϕ_{LC} of 0.5 wt%. When increasing the salt concentration by adding NaCl, ϕ_1 and ϕ_{LC} tended to increase, while the colloid aggregated at higher salt concentrations. In the SAXS results, a peak attributed to the loose lamellar structure with basal spacing of 63 nm was observed at 2.5 wt%. The basal spacing was similar to that estimated from the one-dimensional swelling law. Because the graphene oxide nanosheet has strong luminescent properties, the characterization of the structure was carried out by direct observation by confocal laser scanning microscopy (Fig. 8.14).

Fig. 8.13 Disclination morphologies of graphene oxide liquid crystals. **a** Typical nematic schlieren texture of a 0.3 wt% dispersion with $\pm 1/2$ disclinations and **a** +1 disclination. Successive rotations of crossed polarizers accompanied the rotation of brushes at various rotating rates and directions. **b** SEM image of a graphene oxide liquid crystal in a freeze-dried sample (0.5 wt%). *Blue* and *red* symbols indicate +1/2 and -1/2 disclinations, respectively. Reprinted with permission from Ref. [55]. Copyright 2002 WILEY-VCH



Xu et al. [57] also reported that graphene oxide nanosheets form LC phases with lamellar structures or the twist-grain boundary phases of chiral liquid crystals with long-range chiral frustration. The thickness of the nanosheet was 0.8 nm, and the average particle size was 0.81 μm . By observation of the schlieren texture, the phase transition from the isotropic phase to the nematic phase at 0.23 vol.% was determined. At greater than 0.39 vol.%, the clear and oriented strip-shaped structure similar to the fingerprint-like structure of the cholesteric phase was observed. The chiral spatial arrangement of the graphene oxide nanosheet was verified by the strong signal of circular dichroism in the wide wavelength range from 380 to 800 nm. The graphene oxide nanosheet with liquid crystallinity was injected into an

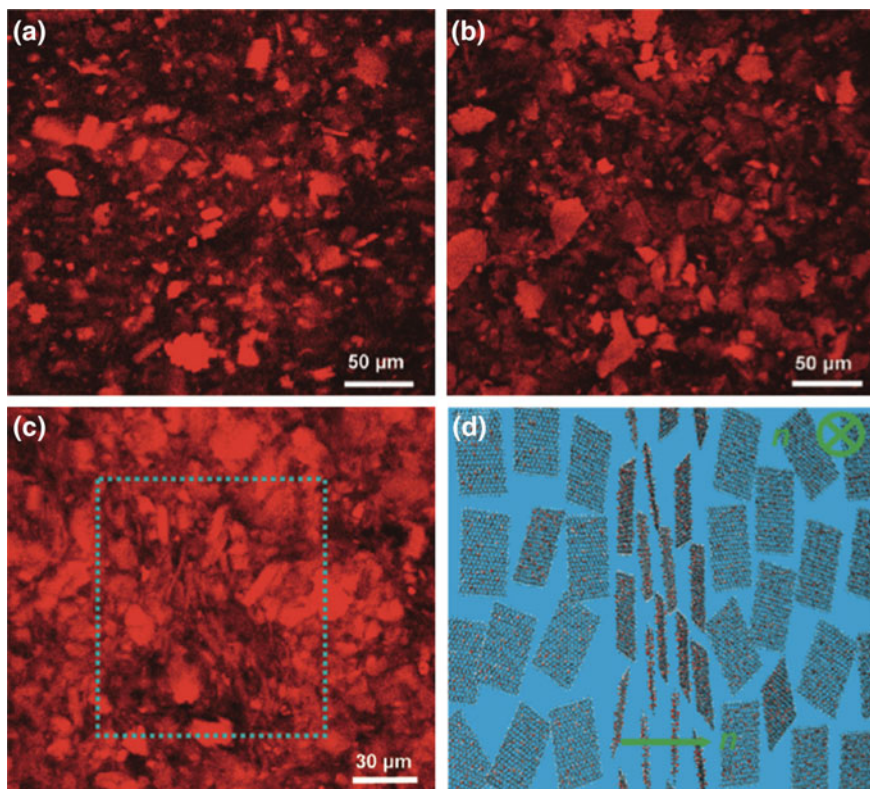


Fig. 8.14 Real-time confocal laser microscopy inspections of GO aqueous dispersions. ϕ is 2.5×10^{-4} (a), 5.0×10^{-3} (b), and 1×10^{-2} (c). A model **d** depicts the rotation of orientation vectors (n) in (c); the arrow directs the vector (n) on the paper, and the *cross* indicates a direction into the paper. Reprinted with permission from Ref. [21]. Copyright 2011 American Chemical Society

NaOH/methanol solution from a syringe, leading to coagulation of the nanosheets as a fiber, which showed high mechanical strength and electrical conductivity.

8.3.5 Other Related Materials

V_2O_5 nanoribbons are obtained by a sol-gel method from a homogeneous solution, not by exfoliation of a layered crystal. The shape is a thin ribbon with a uniform thickness rather than a nanosheet. However, they may be considered a type of nanosheet. The study of the liquid crystal phase of V_2O_5 colloid was first reported by Zocher in the 1920s [58]. In the 1990s, French research groups [59–64] conducted many investigations on the formation of the nematic phase and the response

to electric and magnetic fields [62]. Application to anisotropic media for NMR measurement was also reported [63].

Layered double hydroxides are an important class of layered materials because of their anion exchange capability, in contrast to most of other layered materials with cation exchange capability. Because they are synthesized by a hydrothermal reaction from an aqueous solution of starting chemicals, the particle size and chemical composition are controllable. Although many reports on the exfoliation of layered double hydroxide (LDH) have been published [65–68], it is difficult to obtain fully exfoliated nanosheets with the thickness of 0.6 nm while retaining the large lateral size in high yield. For that reason, there is no report on the liquid crystallinity of exfoliated nanosheets of LDH. However, the liquid crystallinity was reported by several groups for aqueous colloids of unexfoliated Mg/Al-type LDH particles. In 2003, Liu et al. reported that the colloid of LDH microparticles (Mg/Al ratio = 2, average particle size 60 nm, thickness unknown) had a liquid crystal phase at greater than 27 wt% [15]. Wan et al. [69] investigated the LDH with Mg/Al ratio = 1, average particle size of 130 nm, and thickness of 5.5 nm. This system showed the liquid crystal/isotropic biphasic at 10–25 wt%. At 13 wt%, a lamellar structure with basal spacing of 40 nm was identified by SAXS. In the system with Mg/Al ratio = 2, average particle size of 102 nm, and thickness of 7.4 nm, Zhang et al. [70] observed a liquid crystal/isotropic biphasic at concentrations ranging from 16 to 30 wt%. It was also reported that the concentration range shifted to the higher side with increasing salt concentration. Mourad et al. [71] synthesized various LDH microparticles with Mg/Al ratio = 2 with controlled average particle size ranging from 46 to 146 nm. Although the liquid crystal phase was not observed in these systems, the liquid crystal phase appeared when polyisobutylene was added. Zhu et al. [72] and Luan et al. [73, 74] reported that, by adding polymers to LDH microparticles, phase separation to more than three phases was observed. Thus, the formation of the liquid crystal phase of LDH microparticle system requires a higher concentration than other true nanosheet systems (below several %) because they have a low anisotropic ratio of particles due to the low degree of exfoliation.

8.4 Theories for the Liquid Crystal Phase Formation of Nanosheet Colloids

8.4.1 *Onsager Theory*

A theory for the formation of the liquid crystal phase of anisotropic particles, such as rods and sheets, was presented in 1949 by Onsager [27]. In this theory, the formation of a nematic phase, that is, a liquid crystal phase with orientational order and no positional order, is explained by the excluded volume effect on particles. According to this theory, it is expected that the colloid changes from an isotropic

phase to the nematic liquid crystal phase through isotropic-liquid crystal coexistence phase with increasing concentration. This behavior almost corresponds to the observations in experiments. Onsager's theory uses a simple model that assumes only hard core repulsions between cylinder particles with diameter D and height L . Because a particle with $L \gg D$ is regarded as a rod and a particle with $L \ll D$ is regarded as a disc, this theory is applicable for both cases.

When an anisotropic particle is rotating freely by Brownian motion, the particle occupies a very large excluded volume b compared with its solid volume $v_p (= \pi D^2 L/4)$. The ratio of volumes is calculated as follows:

$$\frac{b}{v_p} = \frac{1}{v_p} \frac{1}{4} \pi D \left(L^2 + \frac{1}{2} (\pi + 3) DL + \frac{1}{4} \pi D^2 \right). \quad (8.8)$$

In the limit of $L \ll D$, namely, in the infinitely thin plate particle limit, Eq. 8.8 reduces to:

$$\frac{b}{v_p} = \frac{\pi D}{4 L}. \quad (8.9)$$

In the case of the anisotropy ratio $D/L = 100$, b/v_p is 79. On the other hand, supposing that the particle is not rotating but is perfectly oriented, $b/v_p = 4$. Because of the large difference of b/v_p , large free volume for translational motion is gained if rotation is inhibited. In other words, translational entropy is gained if rotational entropy is lost. Therefore, in the situation that the particles have a large anisotropic ratio, the translational entropy gained by prohibited rotation of the particle, that is, orientation of the particle, should be larger than the rotational entropy lost. Thus, the nanosheets tend to be oriented and form a nematic liquid crystal phase.

Based on this simple theory, Onsager carried out numerical calculations of the transition concentration from the isotropic phase to the isotropic-liquid crystal coexistence phase, ϕ_I , and the transition concentration from the isotropic-liquid crystal coexistence phase-liquid crystal, ϕ_{LC} , and the results are as follows;

$$\phi_I = 3.3 \left(\frac{v_p}{b} \right) = 3.3 \left(\frac{4L}{\pi D} \right) \quad (8.10)$$

$$\phi_{LC} = 4.5 \left(\frac{v_p}{b} \right) = 4.5 \left(\frac{4L}{\pi D} \right) \quad (8.11)$$

As is obvious from these results, the concentration needed for the formation of the liquid crystal phase decreases as the anisotropic ratio D/L increases. Figure 8.15 summarizes the relationship between ϕ_I and D/L for the nanosheet and nanoplate systems reported so far. The trends found in the experimental results are mostly in accordance with the theoretically calculated results.

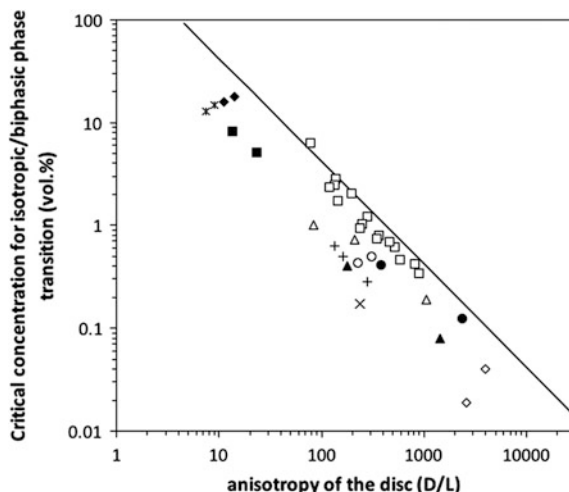


Fig. 8.15 Anisotropy-dependence of the critical concentration for the phase transition from isotropic to isotropic/liquid crystal biphasic observed in disc-like colloidal dispersion systems: (solid line) Onsager's theory, (open square) α -ZrP [28], (open triangle) $K_4Nb_6O_{17}$ [17], (cross) $KCaNb_3O_{10}$ [20], (open diamond) graphite [21, 75], (filled circle) fluorohectorite [22], (filled triangle) fluortetrasilic mica [22], (open circle) beidelite [23], (plus) nontronite [24], (filled square) layered double hydroxide [69, 70], (asterisks) $Ni(OH)_2$ [14, 76], (filled diamond) Gibbsite [12, 13]

Onsager's theory has been modified in various ways through theoretical and simulation approaches. The original Onsager's theory is inaccurate in the case of extremely high concentration because it takes into consideration only two-particle interactions, but multiparticle interactions cannot be ignored at high concentrations. If the multiparticle interactions are taken into consideration, the concentrations of the phase transitions should decrease compared to the original theoretical value [77]. In many cases, nanosheet systems show a large polydispersity of particle size, and this has a great effect. Monte Carlo simulation was carried out on disc-shaped particle systems with polydispersity in particle size. It was shown that the gap between ϕ_I and ϕ_{LC} increases with increasing polydispersity [77]. This theoretical prediction was confirmed experimentally [28]. The flexible shape of nanosheets can also influence the liquid crystal properties. In the experimental and theoretical studies of solution systems of rigid polymers regarded as flexible and long rods, it was revealed that ϕ_I and ϕ_{LC} are larger for polymers with larger flexibility [5]. On the other hand, the emergence of the liquid crystal phase with one-dimensional or two-dimensional positional order, namely, a smectic phase or a columnar phase, was predicted by both theoretical and simulation studies [14]. Experimentally, Lekkerkerker et al. reported the emergence of the columnar phase in ideal experimental systems, such as rod-shaped boehmite particles and plate-shaped gibbsite particles [12]. However, in the nanosheet systems, columnar phases have not been reported due to their very large D/L ratio and large polydispersity.

8.4.2 Other Theories

Provided that the interaction between nanosheets is completely repulsive, considering only the simple Onsager theory is sufficient for understanding the nanosheet liquid crystal systems. However, in many cases, it is not enough. Whereas Onsager's theory and its modified theory explain the emergence of nematic, smectic, and columnar phases, the theories do not explain the liquid crystal phases with swollen lamellar structure and high structural order, which have been observed in many nanosheet liquid crystal systems.

If the repulsive force between nanosheets is strong enough, we can easily guess that nanosheets in the nematic phase form a lamellar structure with the basal spacing predicted by the one-dimensional swelling law of Eq. (8.6). However, in many cases, a smaller basal spacing is observed compared to that predicted by the one-dimensional swelling law. These phenomena can be related to the fractal-like inhomogeneous structure composed of sparse and dense parts of nanosheets in nanosheet colloidal systems. The existence of the fractal structure in nanosheet colloidal systems was noted by many researchers. If the inhomogeneous structure exists, what is the origin of this structure? It is reasonable that relatively strong attractive forces, other than the weak van der Waals attractive force considered in DLVO theory, affect the formation of the fractal structure.

Depletion interaction is thought to be one of the origins of these attractive forces. This interaction is the entropic attractive force induced by the addition of smaller colloid particles to the original colloid. As the distance between two large colloid particles decreases, it becomes difficult for the small particles to be present in the narrow space between the two large colloid particles. As a result, the pressure from the small particles to the large particles works more strongly in the direction that is advantageous to drive the two large particles closer, that is, the attractive force is substantial. Because nanosheet systems have high polydispersity, it is possible that the attractive depletion force from the coexisting smaller nanosheets is working between the larger nanosheets.

The Ise-Sogami theory is also remarkable [78]. According to this theory, attractive forces are acting between the particles with the same type of charge (positive–positive or negative–negative) due to the attractive interaction between a colloidal particle and its counter ion cloud surrounding the particle. Although this theory is different from DLVO theory, which is known as the classical standard, and caused many controversies, this theory can explain the structural formation of spherical colloidal particles and the swelling behavior of layered clay minerals quantitatively. Smally et al. conducted a detailed study on the ideal system in which the single-crystal layered clay mineral vermiculite swelled in aqueous *n*-butylammonium solution. From the calculation based on DLVO theory, the basal spacing calculated from a secondary minimum did not coincide with the experimental results or a minimum did not appear. In contrast, a deep secondary minimum appeared in the potential curve in the calculation based on Ise-Sogami theory. The position of the secondary minimum d_{\min} is represented by the following simple

equation after some approximations, and the calculated values coincided well with the experimental results.

$$d_{\min} = 4\kappa^{-1} \quad (8.12)$$

A similar explanation is also possible in the largely swelling layered ferrotitanate [79, 80] and layered perovskite [81], both reported by Sasaki et al.

The repulsive force originating from the waviness of nanosheets may also be considered. The waviness of layers in a lamellar phase induces an entropic repulsive force known as the Helfrich interaction [82]. In general, the inorganic crystals constructed by covalent bonds have a much higher modulus of elasticity than the well-studied molecular layers composed of surfactant. However, as suggested by the bent-shaped nanosheets formed by drying on a TEM grid [17] and the wrinkles in the nanosheets formed by the elongation and compression of cast nanosheets on a PDMS substrate [83], a nanosheet is not a completely rigid plate but has flexibility to some extent in a solvent. It is thought that the modulus of elasticity of nanosheets is influenced by the chemical composition, thickness of the layers of nanosheets, coexistence of solvent molecules, and counter ions, so that the extent of waviness of a nanosheet also changes depending on these factors. Considering Helfrich interaction, the basal spacing d is expected to show the difference from the one-dimensional ideal swelling behavior as:

$$d = \frac{L A_s}{f A_p} \quad (8.13)$$

Here, A_s is the substantial area of the nanosheet and A_p is the area of a crumpled nanosheet projected from the top. If the nanosheet is crumpled, A_p is smaller than A_s , so the basal spacing is larger than the rigid plane.

8.5 Orientational Control Under External Fields

The colloidal nanosheets can be easily manipulated by external fields. Because of their nature of soft matter, they can change their orientation with weak external forces. This property allows us to construct various hierarchical structures up to macroscopic scale from the nanosheets. We can obtain the desired soft colloidal structures by the controlled application of external fields. Electric and magnetic fields, shear flows, and interaction at interfaces have been examined as external fields. The orientation under an external field is induced by the intrinsic shape anisotropy of the nanosheets. Since the shape anisotropy is accompanied by anisotropy of the dielectric constants and magnetic susceptibilities, the nanosheet orientation can be altered by the external forces even in isotropically dispersed states. However, the nanosheet colloids in the LC state often show specific structures because of the collective nature of LCs.

8.5.1 Orientation Under Electric Fields

The orientation of the nanosheets under electric fields is principally governed by their dielectric anisotropy derived from their 2D shape. Electric field-induced orientational control is applicable for most colloidal nanosheets. The electric alignment of nanosheets was discovered in the 1930s as a birefringence change with the application of continuous AC or pulsed DC electric fields [84–86]. This phenomenon is termed electric birefringence. Because most of the nanosheets bear permanent electric charges, AC electric fields are usually utilized for the continuous application of electric voltages; continuous DC electric fields do not retain the nanosheets in a colloidal state but electrophoretically deposit them on electrodes [87].

8.5.1.1 Electric Birefringence

Electric birefringence is an electrooptic effect that occurs when anisotropic colloidal particles are electrically aligned. Because of their 2D shape, colloidal nanosheets induce large optical retardation to the light propagating along the in-plane direction (Fig. 8.16a). If the nanosheets are lamellarly oriented with a random arrangement with respect to their in-plane direction, the index ellipsoid of the nanosheet colloid can be drawn as optically uniaxial, as in Fig. 8.16b. Birefringence of the colloid consisting of the oriented nanosheets is observed, when the light is not parallel to the n_o axis; that is, the colloid acts as a medium with a uniform refractive index when the incidence of the light is perpendicular to the nanosheet surface [88].

Historically, electric birefringence had been investigated for clay colloids under continuous AC electric fields ($70\text{--}500\text{ V cm}^{-1}$, $50\text{--}10^6\text{ Hz}$ [84–86]) to determine

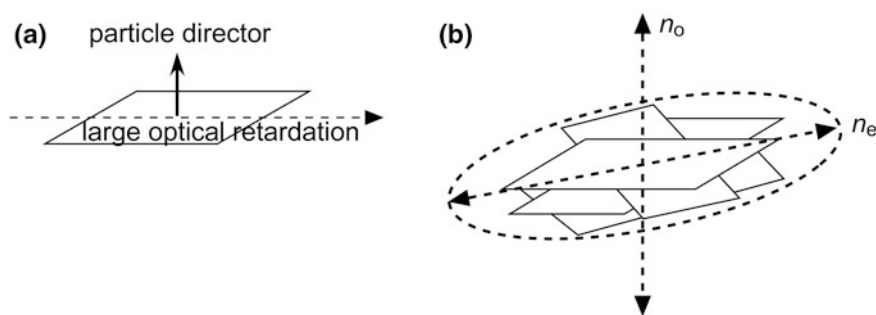


Fig. 8.16 Geometry of the crystallographic and optic parameters related the colloidal LCs of inorganic nanosheets: **a** directions of large optical retardation and particle director for each nanosheet, and **b** proposed orientational ordering of the nanosheets in the LC state and directions of large retardation (n_e) and isotropic (n_o) expected for this ordering. Adapted with permission from [88]. Copyright 2011 American Chemical Society

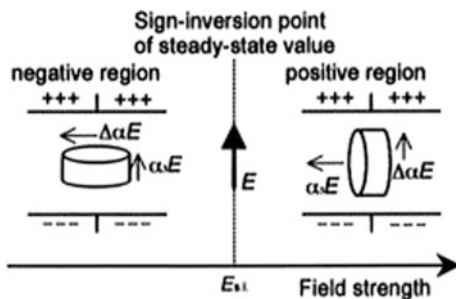


Fig. 8.17 Schematic presentation of particle orientation against field strength for Na-montmorillonite particles. Below the sign inversion field $E_{s,i}$, the plane of the particle is oriented perpendicular to the direction of electric field (*left*). Above $E_{s,i}$, the plane of the particle is oriented parallel to the direction of electric field (*right*). Reprinted with permission from [94]. Copyright 1996 American Chemical Society

the orientation of colloidal anisotropic particles under external fields. Later, pulsed DC electric fields were utilized to extract detailed orientation mechanism by analyzing the temporal response of the nanosheets [89–95]. Because electrically charged nanosheets dispersed in water are accompanied by a huge amount of solvated counteranions, the electrooptic response of the nanosheet colloids can be ascribed not only to the alignment of nanosheets but also to the electrically induced reorganization of the counteranions around the clay nanosheets. Both of the movements occur upon the application of electric voltages with different time constants, and the opposite signs of the electric charges of the nanosheets and counteranions lead to positive/negative inversion of the birefringence (Fig. 8.17) [94]. Because of the different diffusion rate of the nanosheet particles and the surrounding ionic species, their responses to an applied pulsed electric field have a time lag that causes time-dependent sign inversion of the birefringence. Based on such electrooptic behavior, the kinetics of the electric alignment of clay nanosheets has been discussed.

Because the colloidal clay nanosheets can adsorb cationic dyes, the electric alignment of clay nanosheets can be used to align the adsorbed dye molecules. This dye orientation is observed as electric dichroism of the optical absorption due to the supported dye molecules. This phenomenon can be applied for color modification of the colloids and to investigate the binding state of the dyes to the clay nanosheets [96–101].

8.5.1.2 Electrorheological Behavior

The electric response of colloidal particles leads to reversible alterations of the rheological properties of the system upon the application and removal of an electric voltage. This phenomenon is termed the electrorheological (ER) effect [102]. Colloidal systems showing great ER effects have attracted interest as novel smart

fluids applicable for valves, clutches, dampers, and actuators. Layered materials, in particular clay minerals and recently graphene oxide (GO), have been examined as ER materials [103–107].

For ER applications, clay particles are usually not exfoliated but are hydrophobized and dispersed in silicone oil because the ER fluids are typically obtained as colloids of dielectric particles in insulating solvents. Interlayer modification by long-chain organic molecules or polymers is used for this purpose [103–105]. Modification of the external surfaces is also effective, as demonstrated by nanocomposites with inorganic dielectric oxide particles [108] or polymer nanospheres [109]. For GO particles, external surface modifications are mainly employed because they are exfoliated into stacked nanosheets [107, 110–112]. Under the application of an electric field (DC or AC), the modified clay or GO particles are polarized and aggregated into chain-like structures in parallel with the field. When the electric field is applied perpendicular to the flow direction, the chain-like aggregates suppress the flow of the colloid, which is a typical ER response.

However, dried clay particles with hydrophilic inorganic interlayer cations can also be dispersed in silicone oil to show ER effects [106, 113]. As shown in Fig. 8.18, chain-like structures are obtained for clay particles with inorganic interlayer cations. The difference in the structures compared to the interlayer cations indicates a critical role of the interlayer species in the ER properties of the clay minerals. Dried GO particles dispersed in silicone oil also exhibit ER behavior without hydrophobic additives [114].

The ER behavior of the exfoliated clay nanosheets has been examined in water. Aqueous clay colloids show reversible viscosity increase when applying DC or

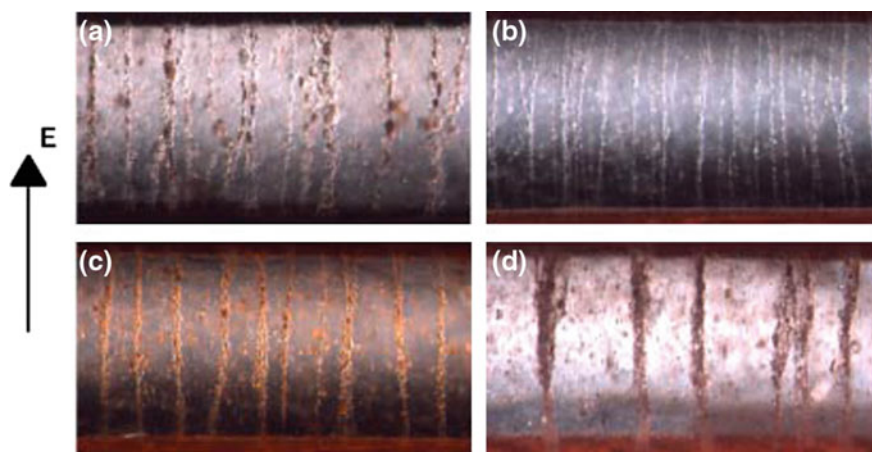


Fig. 8.18 Optical microscope images of electrorheological chain formation in oil suspensions of smectite clays. **a** Na-fluorohectorite. **b** Ni-fluorohectorite. **c** Fe-fluorohectorite. **d** Natural quick clay. Reprinted from [106]. Copyright 2006 EDP Sciences

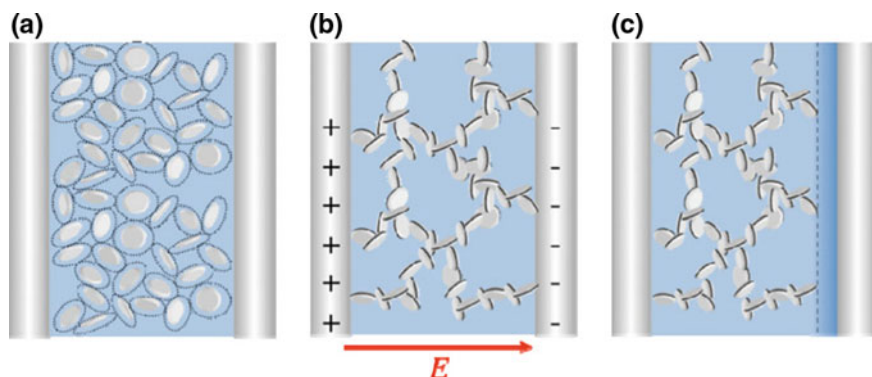


Fig. 8.19 Schematic illustration of dispersion states of hectorite particles in deionized water under steady shear. **a** without the electric field, **b** under the DC electric field, and **c** after removing the electric field. The *broken line* shows a boundary surface of colloidal-rich region and water one. Reprinted with permission from [115]. Copyright 2013 Springer

low-frequency ($\sim 10^{-3}$ Hz) AC voltages [115–117]. Their ER response is characterized by low threshold voltages of less than 100 V cm^{-1} . AC voltages with a frequency greater than 10^{-2} Hz are ineffective. The viscosity increase has been ascribed to the formation of “house-of-cards”-type networks between the clay nanosheets whose structure is not fully relaxed, as indicated by incomplete recovery of the viscosity after the removal of the electric field (Fig. 8.19).

8.5.1.3 Electric Alignment of the Nanosheets in the LC State

Application of electric fields to aqueous nanosheet LCs gives macroscopically ordered nanosheet structures, which can be ascribed to the synergy of the electric and liquid crystalline alignment of the nanosheets. High-frequency AC voltages are generally utilized to align the electrically charged liquid crystalline nanosheets in aqueous systems. The first example of the electric alignment of the nanosheet LCs was reported for the colloids of beidellite clay [23]. When a colloidal LC sample in a 0.2-mm thick and 2-mm wide flat capillary is subjected to an AC voltage of 4000 V cm^{-1} and 500 kHz between electrodes placed in parallel with 1 mm distance in the longitudinal direction of the capillary, the clay nanosheets are aligned in parallel to the electric field to give macroscopic homogeneous ordering of the nanosheets over the area of $2 \text{ mm} \times 1 \text{ mm}$ (Fig. 8.20). AC voltage applications to isotropic and biphasic (coexistence of isotropic and nematic phases) colloids of the same clay mineral (beidellite) also align the nanosheets, and their ordering degree is unexpectedly high compared with those induced theoretically [118]. This behavior is explained by the strong coupling of the electrically charged clay nanosheets and the applied electric field.

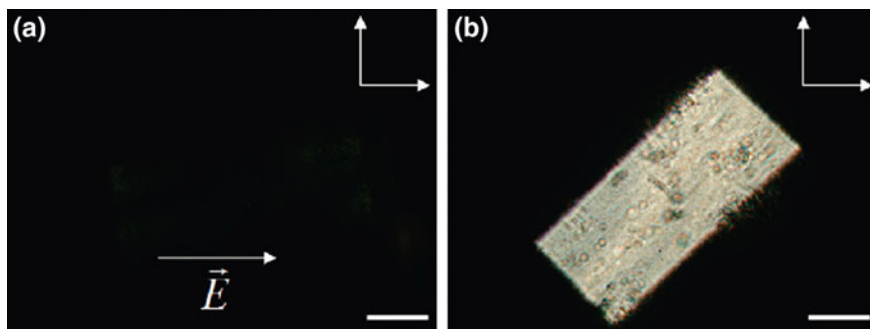


Fig. 8.20 Polarized optical microscope images of fluid nematic samples of beidellite suspensions (ionic strength = 10^{-5} mol L $^{-1}$ and $\phi = 0.61\%$) in a 1 mm cylindrical glass capillary aligned in a 4×10^4 V m $^{-1}$, 500 kHz electric field at **a** 0°, extinction; and **b** 45°, maximum of transmission. The crossed polarizer and analyzer are indicated by the *white arrows*, and the *scale bar* indicates 500 μ m. Reprinted with permission from [23]. Copyright 2009 American Chemical Society

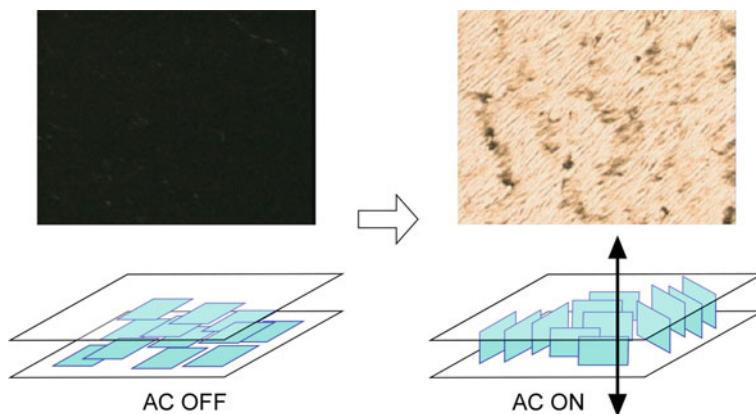


Fig. 8.21 Optical microscope images and schematic representation of the colloidal hexaniobate nanosheets (10 g L $^{-1}$) in LC state (*left*) before and (*right*) after the electric alignment under the AC electric field of 15×10^2 V cm $^{-1}$ and 50 kHz in a 100 μ m thick cell. Adapted with permission from [88]. Copyright 2011 American Chemical Society

The electric alignment of the colloidal LCs of the hexaniobate $K_4Nb_6O_{17}$ nanosheets was examined with AC electric fields of 500–2000 V cm $^{-1}$ and 50 kHz [88]. The electric field is applied to the LC sample placed in a 0.1-mm thick sandwich-type cell in the direction perpendicular to the cell surface. The nanosheets in the LC colloids are aligned parallel to the electric field, i.e., perpendicular to the cell surface, showing a strong electrooptic response (Fig. 8.21). However, in contrast to the beidellite clay system, the electrooptic response of isotropically dispersed nanosheets is much weaker ($\sim 1/1000$) than that of the LC samples. This result indicates a contribution of the collective nature of the LC state to the

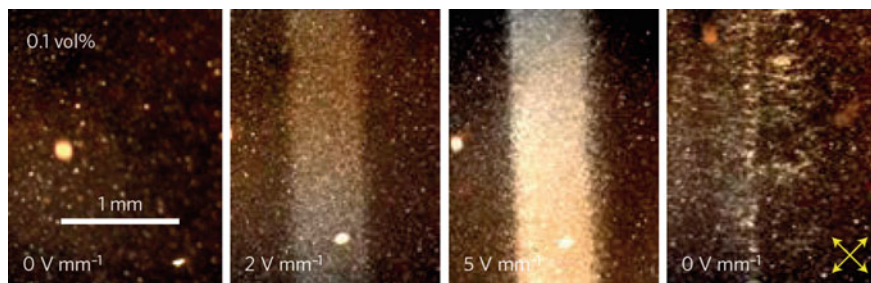


Fig. 8.22 Electric-field-induced birefringence of colloidal GO nanosheets. Field-induced birefringence was generated by applying electric fields (10 kHz) to a cell with thickness of 300 μm thick and distance between the electrodes of 500 μm filled with an aqueous 0.1 vol.% GO dispersion. When the field was switched off, the field-induced birefringence almost disappeared, with only slight nematic aggregation remaining. Reprinted with permission from [75]. Copyright 2014 Nature Publishing Group

nanosheet alignment under the external fields. The electrooptic behavior of the nanosheet LCs is characterized by a slow response and low threshold voltage; the nanosheet alignment shifts in a time range of seconds with a less than 1 V cm^{-1} electric field. This is ascribed to the mesogen size of the nanosheet LCs, which is much larger than that of conventional molecular LCs. Retention of the electrically induced alignment, being a type of a memory effect, is observed for the LCs with high nanosheet concentrations. A macroscopic monodomain structure is obtained by repeated AC voltage applications, which reorient the nanosheets through backflow in the sample cell.

Graphene oxide (GO) nanosheet LCs also show electric alignment under AC electric fields of $10\text{--}200 \text{ V cm}^{-1}$ and 10 kHz [75] (Fig. 8.22). A 0.3-mm thick thin-layer cell is used with electrodes placed in parallel to the cell surface with a 0.5 mm distance. Similar to the niobate system, the GO nanosheet LCs show slow electric response and sensitivity to low electric fields. The electrooptic response also depends on the concentration of coexisting ionic species [119]. The electric response of the colloidal LCs were lost with $10^{-3} \text{ mol L}^{-1}$ of NaCl or HCl, while NaOH did not have large effect. This behavior is explained by the modification of the electric charges on the GO nanosheet surfaces in the presence of coexisting electrolytes, depending on their concentration and species; the surface charge alters the polarization of the nanosheets to change their electrooptic response.

8.5.2 Orientation Under Magnetic Fields

Similar to the electric fields, magnetic fields align colloidal nanosheets. Magnetic alignment is easily attained when the nanosheets contain magnetic elements. Nanosheet colloids of nontronite clay, which contains Fe(III) species in the

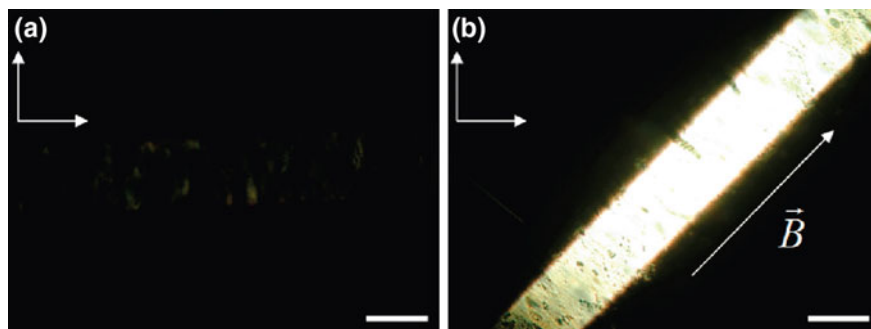


Fig. 8.23 Polarized optical microscope images of a fluid nematic phase of a beidellite suspension at an ionic strength of 10^{-4} mol L $^{-1}$ and $\phi = 0.62\%$ held in a 1 mm cylindrical glass capillary and submitted to an 8 T magnetic field for 15 h. Photographs were taken at **a** 0° , extinction, and **b** 45° , maximum of transmission. The crossed polarizer and analyzer are indicated by the *white arrows*, whereas the *scale bar* represents 1 mm. Reprinted with permission from [23]. Copyright 2009 American Chemical Society

aluminosilicate layers, show magnetic alignment [49, 120]. The nontronite nanosheets in the isotropic and LC states are both aligned under a magnetic field of >1 T, and their free and collective orientations are distinguished by ^2H -NMR analysis. When the nanosheets are diamagnetic, more intense magnetic fields are required. Examples are nanosheet LCs of layered metal phosphate $\text{H}_3\text{Sb}_3\text{P}_2\text{O}_{14}$ and beidellite clay (Fig. 8.23), which are aligned under magnetic fields of 19 and 8 T, respectively [16, 23]. Platy particles of non-exfoliated hexaniobate $\text{K}_4\text{Nb}_6\text{O}_{17}$, as well as nanoscrolls obtained from its exfoliated nanosheets, are magnetically aligned at 12 T [121]. Because GO and reduced GO (rGO) have rather high magnetic susceptibilities among the diamagnetic materials due to their π -conjugated systems, their nanosheets can be aligned slowly under relatively weak magnetic fields of ~ 0.25 T [55, 122]. However, nanosheet LCs of synthetic fluorohectorite clay characterized by large nanosheet size and the absence of magnetic elements have been reported to show magnetic alignment at 2 T [123], which could be ascribed to the collective nature of the large-size nanosheets in the LC state.

Another technique for the magnetic alignment of the diamagnetic nanosheets is loading magnetic nanoparticles, such as Fe_3O_4 , on the nanosheets. Partly restacked few-layer nanosheets of perovskite-type niobate $\text{HCa}_2\text{Nb}_3\text{O}_{10}$ are oriented under magnetic fields greater than 10^{-3} T [124, 125] when Fe_3O_4 nanoparticles are attached via covalent linkers. The 2D distribution of the magnetic nanoparticles on the nanosheets leads to biaxial superparamagnetic susceptibility of the colloidal particles, which are aligned parallel to the magnetic fields. GO and reduced GO nanosheets also become easily aligned magnetically with this method [55, 126].

8.5.3 Orientation by Shear Forces

The alignment of the colloidal nanosheets is also achieved under shear. The application of shear forces to the colloids induces nanosheet orientation along the shear direction. A typical example is observed during settlement of the colloidal nanosheets. Nanosheet alignment along gravity at a macroscopic (\sim cm) scale has been reported for the colloidal LC of hexaniobate $\text{K}_4\text{Nb}_6\text{O}_{17}$ nanosheets placed in a test tube (1 cm in diameter) [30] (Fig. 8.24). This behavior is explained by the flow of the colloids induced by the settlement of the dispersed nanosheets with gravity.

The flow-induced orientation is observed more clearly by applying mechanical shear to the nanosheet colloids. When a test tube containing a hexaniobate nanosheet colloid is rotated, the colloid shows birefringence along the shear flow, indicating the shear-induced orientation of the nanosheets [17, 30]. The flow birefringence is observed for both isotropic and LC nanosheet colloids. The shear-induced alignment is temporal and gradually disappears after removal of the rotation. This phenomenon has also been observed for nanosheet LCs of montmorillonite clay [25] and GO [127]. The relaxation of the shear-induced alignment becomes slower at higher nanosheet concentrations.

The shear-induced alignment of the nanosheets has been applied for the preparation of practical materials. The preparation of self-supporting films is a known example. Casting the colloidal nanosheets on a flat substrate causes unidirectional deposition of the nanosheets, and self-supporting “paper” is obtained after

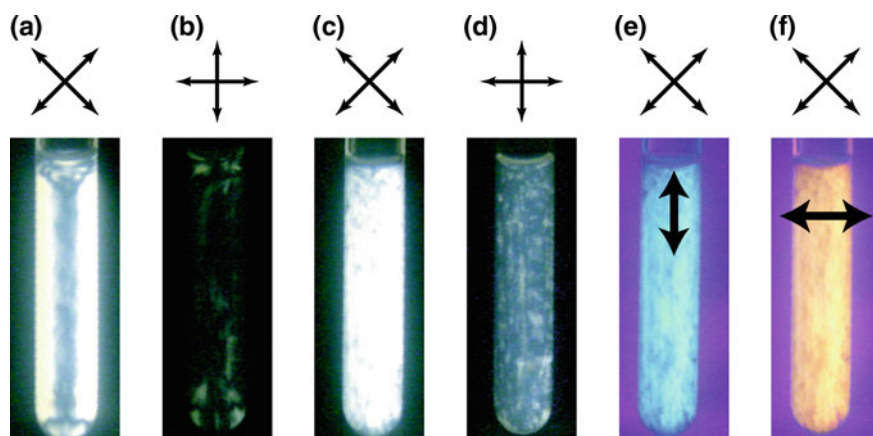


Fig. 8.24 Photographs of the hexaniobate nanosheet colloid containing $9.6 \times 10^{-5} \text{ mol L}^{-1}$ of $[\text{Nb}_6\text{O}_{17}]^{4-}$ in a test tube (1 cm in diameter) observed between crossed polarizers whose directions are indicated by double arrows. The images were taken after several seconds of rotation for **a** and **b** and after letting the sample stand for 60 min for **c–f**. A 1st-order retardation plate (optical retardation = 530 nm) was used in observations **(e)** and **(f)**, setting the “slow-vibrational direction” as indicated by the **bold arrows**. Reprinted with permission from [30]. Copyright 2002 WILEY-VCH

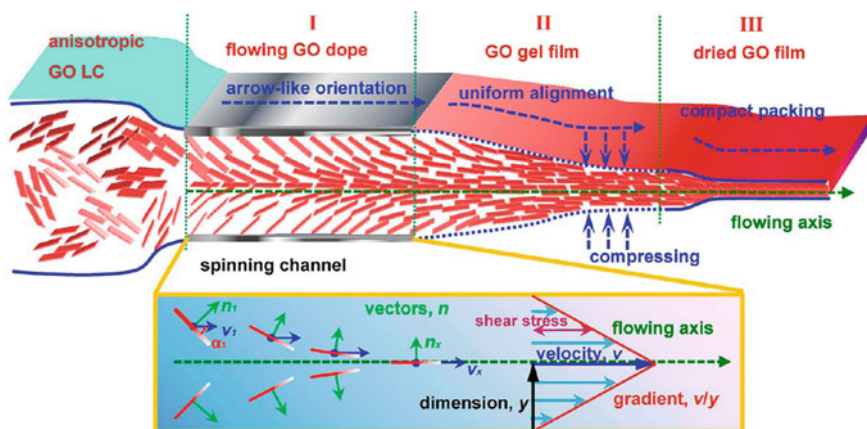


Fig. 8.25 Schematic diagram depicting the structural evolution of GO paper with three typical stages: *I*, arrow-like orientation; *II*, uniform alignment; *III*, compact packing. Here, n , v , and α denote the orientation vector of GO, the velocity of the flowing layer, and the angle between the GO sheets and the flowing direction, respectively. Reprinted from [128]. Copyright 2014 American Chemical Society

removing the substrate. While “clay papers” are utilized as colorless transparent supports of functional dyes [129, 130], films of semiconducting oxide nanosheets work as “photocatalytic paper” [131]. “Graphene papers” prepared from GO or rGO nanosheets have been investigated as membranes for adsorption and separation (Fig. 8.25) [128, 132, 133]. On the other hand, fiber-spinning of mixtures of colloidal GO or rGO nanosheets with organic polymers yields inorganic–polymer composite fibers [134–136]. The strong shear forces applied during the spinning process align the nanosheets in the fibers to give strong mechanical strength and physicochemical properties such as electrical conductivity due to graphene.

8.5.4 Hierarchical Macroscopic Structures of Nanosheet LCs Under Dual External Fields

The 2D shape and large particle (mesogen) size of the nanosheet LCs enable the organization of various hierarchical nanosheet-based structures at the macroscopic scale. In contrast to 1D particles (rods) that are unidirectionally aligned with a single external force, 2D particles have two orthogonal axes for regulation of their alignment so that unidirectional alignment is only attained under dual external fields. The large particle (mesogen) size of the nanosheets at the μm level is advantageous for constructing macroscopic structures hierarchically, in comparison with conventional molecular LCs.

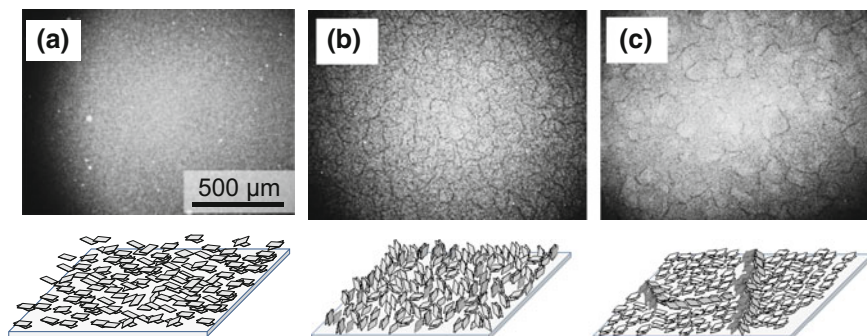


Fig. 8.26 Gray-scaled FOM images and schematic representation of the nanosheet arrangement of the niobate nanosheet LC (5 g L^{-1}) in a $100\text{-}\mu\text{m}$ thick cell before **a** and after incubation for **b** 60 and **c** 120 min. Adapted with permission from [137]. Copyright 2014 The Royal Society of Chemistry

Based on this consideration, we have organized the hierarchical macroscopic structures in the colloidal LCs of hexaniobate $\text{K}_4\text{Nb}_6\text{O}_{17}$ nanosheets [137]. An important key for the hierarchical organization is the growth of LC domains, called tactoids, as the secondary building blocks followed by controlled application of external fields. The growth of the tactoids is achieved by keeping the nanosheet LCs stand at room temperature, a process called incubation, for several tens of minutes (Fig. 8.26). The tactoid growth is analogous to Ostwald ripening in crystal growth.

The tactoids are then assembled into macroscopic higher order structures with characteristic lengths of sub-mm to mm under simultaneous application of an AC electric field and gravity, whose directions determine the final structural motif. Although a net-like structure forms when applying the electric and gravitational forces in the same direction, a stripe structure, where the nanosheets are unidirectionally aligned, is obtained when the electric field is applied in the direction perpendicular to gravity (Fig. 8.27). The use of well-grown tactoids is a key to macroscopic structural control. Among these macroscopic structures of the photocatalytically active niobate nanosheet LCs, the stripe structure is applicable to control the photocatalytic reactions. The nanosheet stripes exhibit photocatalysis, which reflects the alignment of the nanosheets with respect to the polarized direction of the impinging light.

8.5.5 Orientation at the Interfaces

Although the inorganic nanosheets are well dispersed in aqueous and organic liquid phases when they are sufficiently hydrophilic or organophilic, respectively, the particles can be accumulated at heterogeneous interfaces if they have appropriate affinity to all the related phases. Typically, a small amount of long-chain

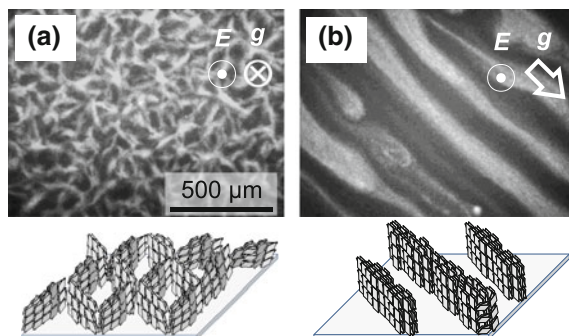


Fig. 8.27 Gray-scaled FOM images and schematic representation of the nanosheet arrangement of the niobate nanosheet LC (5 g L^{-1}) in a $100\text{-}\mu\text{m}$ thick cell under an AC electric field of 5 V cm^{-1} and 50 kHz after incubation for 120 min. The electric field was applied in the direction **a** parallel and **b** perpendicular to gravity for 8 and 60 min, respectively. The directions of the electric field (E) and gravity (g) are indicated by circles and an arrow. Adapted with permission from [137]. Copyright 2014 The Royal Society of Chemistry

organoammonium salt dissolved in an organic solvent is carefully spread on the surface of an aqueous nanosheet colloid to yield a nanosheet monolayer at the air–water interface [138, 139]. Another method of preparing an interfacial monolayer reported for synthetic saponite clay is intercalation of the organoammonium species and subsequent dispersion in an organic solvent, which is then spread on water [140]. Interfacial monolayer films have been fabricated into nanosheet multilayer films through the Langmuir–Blodgett technique.

Solid particles can stabilize interfaces when they are trapped there [141, 142]. This property is applicable to stabilizing liquid and gas droplets that are colloiddally dispersed in continuous phases. Such colloidal systems of particle-stabilized droplets in continuous phases are termed Pickering emulsions (liquid in liquid) and foams (gas in liquids), and liquid marbles (liquid in air) [143, 144]. These colloidal systems provide broad practical applications in various fields, such as the petroleum, food, cosmetic, and pharmaceutical industries and are recognized as a type of multicomponent soft matter where particles are aggregated in a specific manner at structured interfaces. Inorganic particles can add unusual properties to such materials if the particles possess advanced optic, photochemical, catalytic, electric, and magnetic properties.

Particles with various morphologies have been examined as such “particle surfactants” [146]; 2D particles can effectively stabilize the interfaces if they are adsorbed in parallel to the interfaces (Fig. 8.28) [145, 147, 148]. In this regard, the exfoliation of layered crystals into nanosheets is not an essential requirement. In fact, non-exfoliated particles of layered crystals with platy morphologies have been employed for Pickering emulsions [145, 148–155] and foams [156–159], where moderately hydrophobic surfaces are required for droplet stabilization. The affinity to the droplet and continuous phases is adjusted by mixing with additives or intercalation of appropriate species into the interlayer spaces. Very recently,

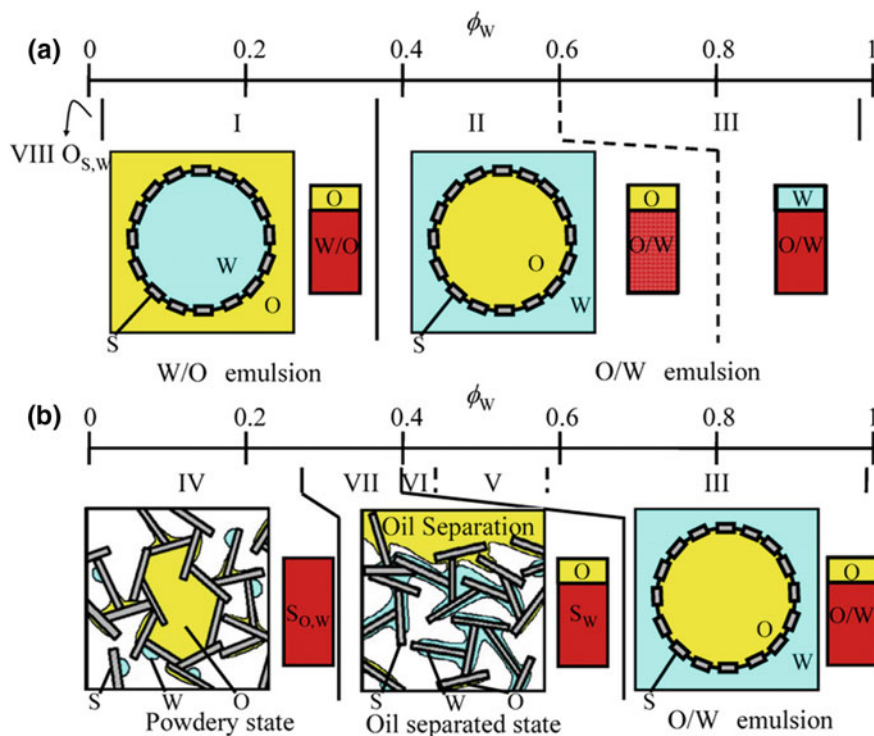


Fig. 8.28 Schematic illustrations of the mixed states of the ternary system consisting of platy clay particles, silicone oil, and water when **a** $0 < \alpha < 0.4$ and **b** $0.4 \leq \alpha < 1$. Reprinted with permission from [145]. Copyright 2009 Elsevier

few-layer GO nanosheets were used to prepare both emulsions and foams after suitable modification of their surfaces (Fig. 8.29) [160–163]. α -ZrP nanosheets also stabilize Pickering emulsions and foams [147, 164].

8.5.6 Immobilization of Aligned Nanosheet Structures

Immobilization of the nanosheet colloid structure regulated by LC phase formation or external field is important for many applications. Inorganic nanosheets, especially clay minerals, have been immobilized in polymer matrix and utilized as nanofillers for plastic polymer materials to improve the thermal stability, gas-barrier properties, and mechanical properties. Recently, nanosheets were also utilized as the fillers for polymer gels, which are network-type polymers swollen by a solvent. The gel materials are applicable for biomaterials and soft actuators. In 2002, Haraguchi et al. [165] reported that the mechanical properties of polymer gels are

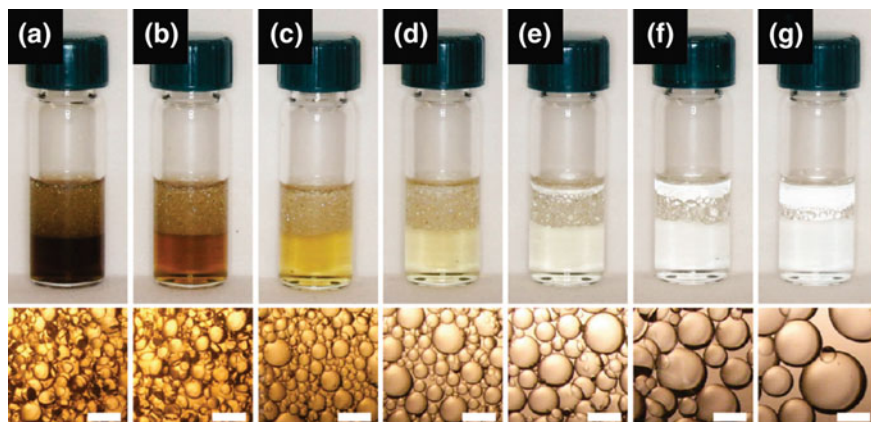


Fig. 8.29 GO at the liquid–liquid interface. GO sheets can stabilize oil droplets in water by adsorbing at the oil–water interface, forming Pickering emulsions. Toluene droplets formed upon shaking a toluene/GO water mixture, where the concentration of GO was varied from **a** 0.95 mg/mL to **b** 0.47, **c** 0.19, **d** 0.095, **e** 0.047, **f** 0.019, and **g** 0.0095 mg/mL, respectively. The *bottom row* shows microscopy images of the toluene droplets. All *scale bars* are equal to 1 mm. Reprinted with permission from [162]. Copyright 2010 American Chemical Society

largely improved by using synthetic hectorite nanosheets as the multiple physically crosslinking sites for polymer chains. Many studies with similar concepts have been reported [166–170]. The synthesis of composite gels was also carried out by photopolymerization, which allows easier control of the shape of the gels [167, 171–173].

Whereas isotropic nanosheet colloids were used in the above examples, composite materials with liquid crystalline nanosheets are expected to show better mechanical and anisotropic properties. Miyamoto et al. [174] reported the composite gel with anisotropic properties, which was synthesized using liquid crystalline clay nanosheets. An aqueous mixture of liquid crystalline fluorohectorite nanosheets, a monomer, a chemical crosslinker, and a radical initiator was flowed into glass capillary, allowing the nanosheets to be macroscopically ordered along the glass wall of the cell used for the synthesis. After polymerization and crosslinking in the capillary, the composite gel was obtained, which contained the nanosheets aligned in a tree-ring-like structure. In this report, the structural analysis during the synthetic process was carried out by SAXS (Fig. 8.30). Before the reaction started, the lamellar structure with the basal spacing of 35 nm was confirmed. The basal spacing decreased as the reaction proceeded, and it was 10 nm at the end of the reaction. After the reaction, the gel was placed in pure water and swelled macroscopically until the equilibrium swelling state. Corresponding to the macroscopic swelling, the basal spacing increased to more than 100 nm. Throughout these processes, the SAXS profile was kept anisotropic. These results confirmed that the polymerization proceeded, maintaining a well-dispersed, liquid crystal state of the nanosheets. Induced by the anisotropic structure, the gel showed

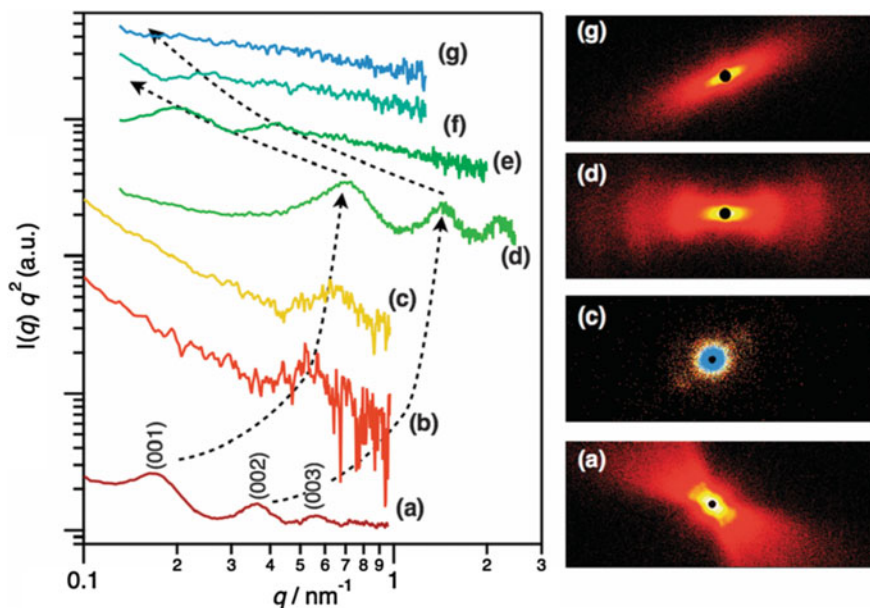


Fig. 8.30 SAXS profiles of the F5-B0-gel system: *a* FHT–NIPA–water mixture (before polymerization), the mixture during polymerization, *b* 1 and *c* 10 min after reaction initiation), *d* as-prepared gel, and the gel swollen for *e* 15, *f* 30, and *g* 60 min in water. Reprinted with permission from Ref. [174]. Copyright 2014 The Royal Society of Chemistry

anisotropic refractive index, modulus of elasticity, mass transport, and thermally induced phase transition behavior.

However, the tree-ring-like ordered structure in this system is not suitable for detailed evaluation of the anisotropic properties and for applications. Miyamoto et al. synthesized a sheet-shaped gel with a centimeter-scale ordered monodomain structure by applying alternating electric field during the synthesis. The orientation was controlled in both the out-of-plane and in-plane directions (Fig. 8.31) [173]. The gel sheet was easily printable with a tetravalent cationic dye at a resolution of tens of micrometers (Fig. 8.32a). When the gel was irradiated with light, only the colored part of the gel was heated, and the gel transformed into an asymmetric shape (Fig. 8.32b) through the thermally induced volume phase transition of PNIPA. This behavior is suitable for soft actuator applications.

Following the above reports, Mejia et al. [175] and Aida et al. [176, 177] reported anisotropic composite gels synthesized in a similar manner. Mejia et al. reported a composite of α -ZrP nanosheets and poly(acrylamide-co-*N*-isopropylacrylamide). They found that the equilibrium swelling ratio and the size of the oriented domain are controllable by tuning the synthetic conditions. Aida et al. used titanate and niobate nanosheets and magnetic field to obtain macroscopically aligned gels. Very large anisotropies in the optical, rheological, and deformation behavior were demonstrated.

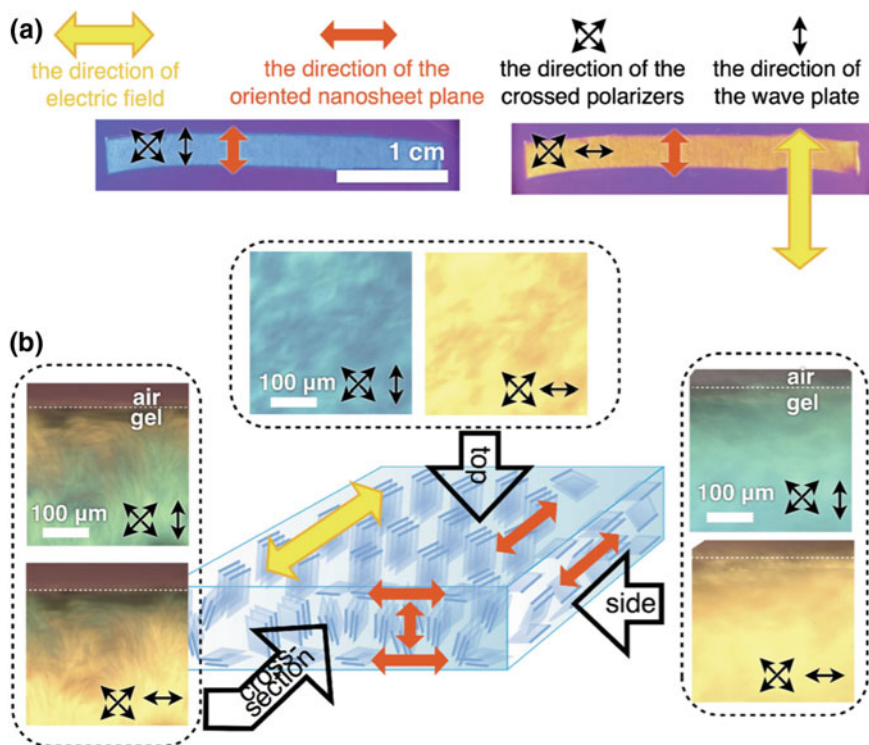


Fig. 8.31 **a** Photographs and **b** microscopic images and schematic structures of the FHT/PNIPA gels containing 1wt% of FHT synthesized with in-plane electric field. The images are observed with crossed polarizers and a wave plate. Reprinted with permission from Ref. [173]. Copyright 2014 WILEY-VCH

8.6 Multicomponent Nanosheet Colloids

8.6.1 Phase Separation in Multicomponent Colloids

The addition of other particles to the nanosheet colloids to yield multicomponent colloids is an important strategy for extracting specific functions from nanosheet-based colloidal systems by utilizing physicochemical interactions between the colloidal particles. In general, multicomponent colloids containing more than two morphologically different particle species, such as plate–rod, plate–sphere, and rod–sphere [72, 74, 178–188], show phase separation, which is demixing of the morphologically different colloidal particles based on entropically driven depletion effects. The phase separation results in rich phase behavior, which is typically observed as the coexistence of plural LC phases [189]. The phase separation of multicomponent colloids involving nanosheets or plate-like particles has been studied theoretically rather than experimentally. Computational studies

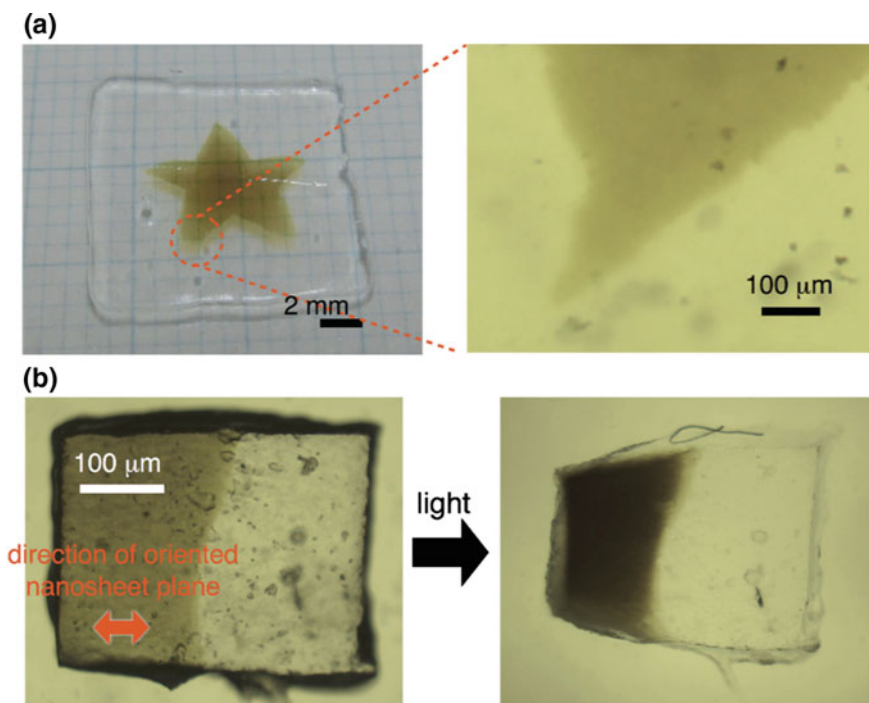


Fig. 8.32 Patterned coloration of the FHT/PNIPA gels with TMPyP dye and its partial photoresponsive deformation: **a** photograph (*left*) and microscopic image (*right*) of the gel printed with the dye pattern; **b** photoinduced partial deformation of the gel partially adsorbed with dye, as observed by optical microscopy. The *red arrow* indicates the direction of the oriented nanosheet planes. Reprinted with permission from Ref. [173]. Copyright 2014 WILEY-VCH

have clarified the multiphase coexistence in plate–rod and plate–sphere systems [190–196]. Additionally, there are theoretical studies of a plate–plate system [197–200], which is a model of the binary nanosheet LCs, indicating three-phase coexistence of one isotropic and two LC phases.

These theoretical predictions have been proved by experimental results, although the real systems are rather complicated because of the presence of particle size distributions and interparticle chemical interactions. For example, an experimental binary system of gibbsite ($\text{Al}(\text{OH})_3$) plates and boehmite (AlOOH) rods shows five-phase coexistence (isotropic, rod-dominant nematic, plate-dominant nematic, unidentified nematic, and columnar phases), in accordance with theoretical considerations (Fig. 8.33) [179, 201]. The plate–polymer systems of gibbsite with poly(dimethylsiloxane) [202] and LDH with poly(ethylene glycol) [72] exhibit the coexistence of four to five phases (one isotropic and three to four LC). An LDH–polymer (poly(vinyl pyrrolidone) binary system shows six-phase existence (one liquid, two isotropic, two LC, and one sediment) [74].

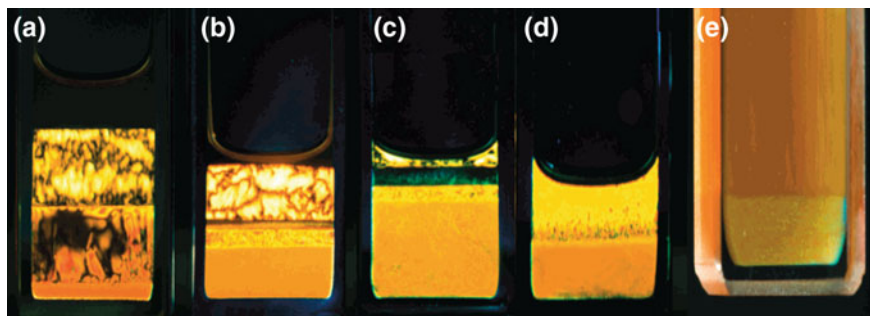


Fig. 8.33 Phase-separated rod-plate mixtures as observed between crossed polarizers. Depicted are **a** four-phase $I + N^+ + N^- + C$ coexistence (denoted in order from *top to bottom*) in a sample with the composition $(\phi_{\text{rod}}, \phi_{\text{plate}}) = (0.06, 0.26)$, **b** five-phase $I + N^+ + X + N^- + C$ coexistence at $(0.10, 0.22)$, **c** four-phase $N^+ + X + N^- + C$ coexistence at $(0.07, 0.29)$, and **d** two-phase $N^- + C$ coexistence at $(0.03, 0.35)$. Image **e** depicts a sample at $(0.02, 0.35)$ exhibiting $N^- + C$ coexistence, photographed without crossed polarizers but illuminated by white light to demonstrate the Bragg reflections in the lower (C) phase. Reprinted with permission from [201]. Copyright 2000 American Chemical Society

With respect to multicomponent colloids involving exfoliated nanosheets, binary systems of the nanosheets and silica spheres have been examined, and their phase behavior is somewhat different from that of conventional plate–sphere systems. The beidellite clay–silica system shows only isotropic–nematic biphasic coexistence, similarly to the single beidellite system; however, introduction of silica particles accelerates the phase separation process [204]. In addition, the silica spheres suppress the sol-gel transition of the clay colloid to stabilize the nematic sol state. Binary colloids of α -ZrP nanosheets and silica particles show multiphase coexistence characterized by isotropic–isotropic demixing; isotropic–isotropic biphasic and isotropic–isotropic–nematic triphasic coexistence is observed (Fig. 8.34) [203]. Isotropic–isotropic phase separation is also observed for a binary system composed of synthetic hectorite clay (Laponite) nanosheets and Fe_2O_3 spherical nanoparticles [205]. A plate–rod system of montmorillonite clay nanosheets and sepiolite clay rods shows three-phase coexistence (one isotropic and two nematic) [206].

8.6.2 Phase Separation of Binary Nanosheet Colloids

In contrast to the plate–sphere and plate–rod systems, plate–plate binary colloids have not been thoroughly explored experimentally. Binary nanosheet colloids prepared from chemically different layered crystals are important members. In addition to the nanosheet systems, an example is a single-component colloid of gibbsite plates with a bimodal distribution of the particle thickness, which exhibits triphasic coexistence of an isotropic, nematic, and columnar phase, and the result is rationalized by computer simulation [200].

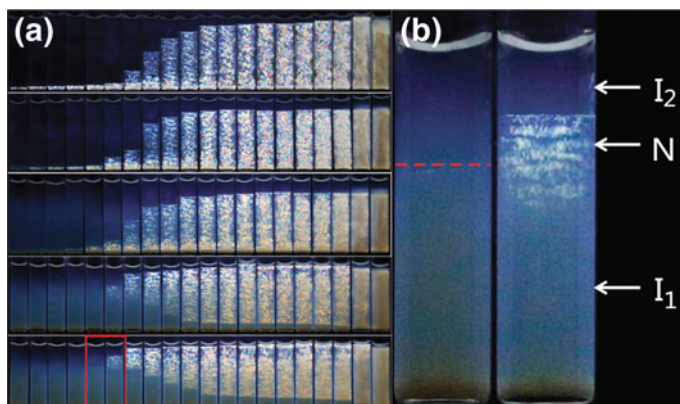
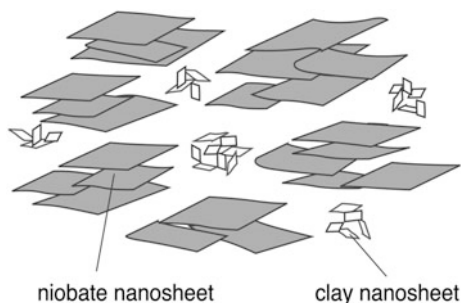


Fig. 8.34 **a** Images of plate–sphere mixtures of α -ZrP nanosheets and silica spheres observed between crossed polarizers 30 days after preparation. From *top* to *bottom*, volume fraction of added silica spheres in percentage is 0, 0.050, 0.230, 0.450, and 0.680, the error bar of which is ± 0.003 . From left to right, volume fraction of ZrP in percentage is 0.36, 0.42, 0.48, 0.54, 0.6, 0.66, 0.72, 0.78, 0.84, 0.9, 1, 1.1, 1.2, 1.3, 1.4, 1.5, 1.7, 2, and 3, 4; the error bar is ± 0.01 . **b** Detail of the two samples boxed in **(a)**, showing I–I demixing and tri-phase coexistence. Reprinted with permission from [203]. Copyright 2015 The Royal Society of Chemistry

Fig. 8.35 Schematic representation of the microscopic phase separation in the niobate–clay binary nanosheet colloids



We have developed binary nanosheet colloids of niobate $K_4Nb_6O_{17}$ and smectite-type clay (natural montmorillonite or synthetic hectorite (Laponite)) nanosheets [207–209]. Although the binary nanosheet colloids are apparently homogeneous at the macroscopic ($>$ sub-mm) scale and show liquid crystallinity, phase separation at the microscopic scale is evidenced by the SAXS analysis, which indicates compression of the LC phase due to the niobate nanosheets with the introduction of clay nanosheets. The niobate and clay nanosheets are separated and assembled into the microdomains of niobate and clay, respectively, as schematically shown in Fig. 8.35. Spectroscopic observations using a cationic organic dye as a probe also support demixing of the clay and niobate nanosheets at the microscopic

level. Based on the result that the cationic dye molecules are selectively adsorbed on the clay nanosheets and the dye does not show spectral dichroism, the clay particles are isotropically dispersed in the binary colloids to be phase-separated from the LC niobate nanosheets.

However, the binary colloids of titanate nanosheets from lepidocrocite-type layered oxide $H_{1.07}Ti_{1.78}O_4$, used instead of the niobate nanosheets combined with the clay nanosheets, result in different phase separation behavior [210], although the niobate and titanate nanosheets have similar geometric shapes and chemical properties. The titanate–clay binary LCs show macroscopic phase separation with three-phase coexistence of one isotropic and two LC phases (Fig. 8.36). The difference between the titanate and niobate nanosheets is due to the different counterions that are introduced as exfoliating reagents for the mother layered crystals: propylammonium for the niobate and TBA^+ for the titanate. Chemical interactions between the titanate and clay nanosheets, mediated by their counterions, destabilize the colloid. Although most of the nanosheets bear permanent surface charges accompanied by counterions, this fact is usually ignored in the simulations so that combination of the nanosheets with different counterions will modify the phase separation behavior.

Binary aqueous nanosheet colloids composed of synthetic hectorite (Laponite) and natural montmorillonite, which are both clay minerals with similar physicochemical properties and different particle sizes, show isotropic–isotropic biphasic coexistence in a mixed gel state [211]. The phase separation occurs at a microscopic scale, similarly to the niobate–clay system, due to kinetic arrest by the gel state (Fig. 8.37). DLS measurements suggest that the montmorillonite nanosheets form a matrix for the hectorite nanosheets by interacting with each other [212].

There are some other nanosheet–nanosheet binary systems with colloidal properties and applications. Reduced graphene (rGO) nanosheets are colloiddally stabilized in the presence of montmorillonite clay nanosheets due to hydrogen-bonding interactions between the rGO and clay nanosheets [213]. The stabilized colloidal nanosheets are applicable for preparing highly oriented hybrid films. The addition of montmorillonite clay nanosheets to a colloidal LC of GO nanosheets enables preparation of graphene–clay hybrid fibers through wet spinning in the presence of an appropriate organic polymer [214]. The hybrid fiber shows superior electric conductivity and thermal stability in air compared with neat graphene fibers due to the suppression of graphene oxidation by the clay nanosheets. Nanosheet–polymer hybrids with two nanosheet species have recently been explored for various applications, such as self-healable hydrogels, artificial nacre, and electrodes [215–217]. A binary system of rGO and manganate nanosheets was found to be stable at limited nanosheet concentrations and aggregated under other conditions [218], as observed for the titanate–clay system. Aggregation is a common phenomenon of binary colloids of nanosheets with opposite electric charges, such as the clay–LDH and GO–LDH systems [219–223].

Fig. 8.36 **a** Phase diagram of the titanate–clay binary nanosheet colloids and typical appearances of the **b** flocculated, **c** isotropic–LC biphasic, and **d** isotropic–LC–LC triphasic samples between crossed polarizers. *Symbols* embedded in the diagram indicate the experimentally examined composition. Reprinted with permission from [210]. Copyright 2014 The Royal Society of Chemistry

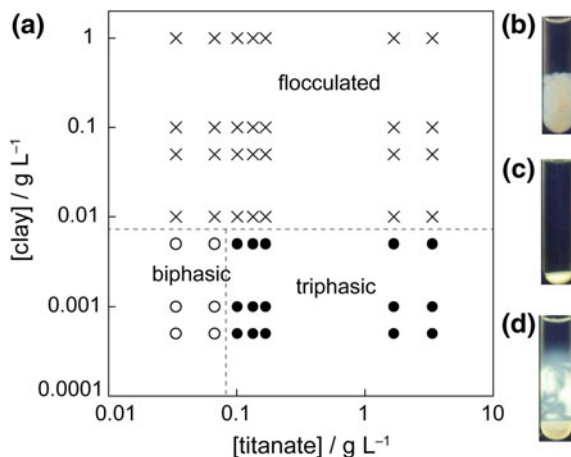
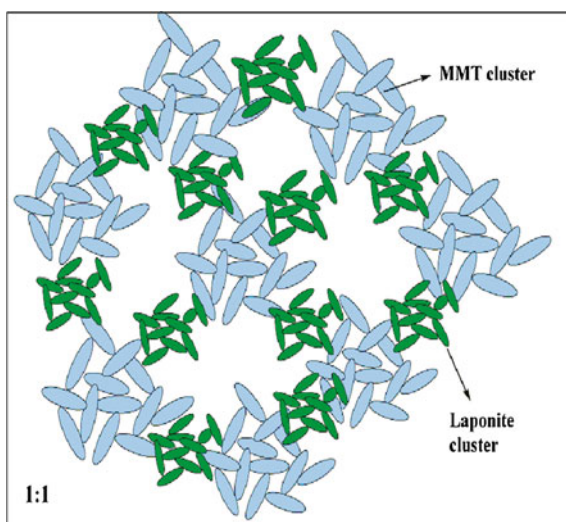


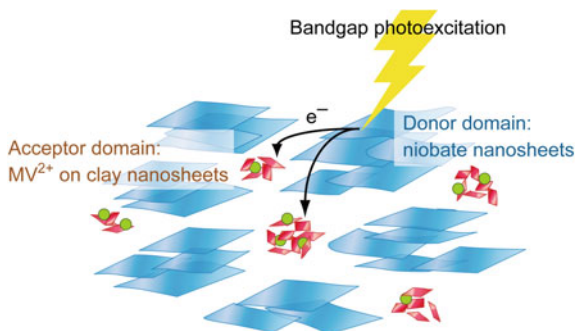
Fig. 8.37 Model of the assembled network structure of the plate–plate binary colloid composed of hectorite (Laponite) and montmorillonite (MMT) nanosheets at a mixing ratio of 1:1. Reprinted with permission from [211]. Copyright 2011 The American Chemical Society



8.6.3 Photochemical Applications of Niobate–Clay Binary Nanosheet Colloids

Niobate–clay binary nanosheet colloids that are phase separated at a microscopic scale can be applied for photofunctional systems. In such systems, photocatalytically active semiconducting niobate and physicochemically inert clay nanosheets are spatially separated but contact easily because the nanosheets are diffusive in the colloidal system and demixed only at a microscopic scale. Selective adsorption of cationic organic molecules onto the clay nanosheets leads to the existence of two

Fig. 8.38 Schematic representation of the photoinduced electron transfer in the MV^{2+} /niobate–clay colloids. Reprinted with permission from [209]. Copyright 2009 American Chemical Society



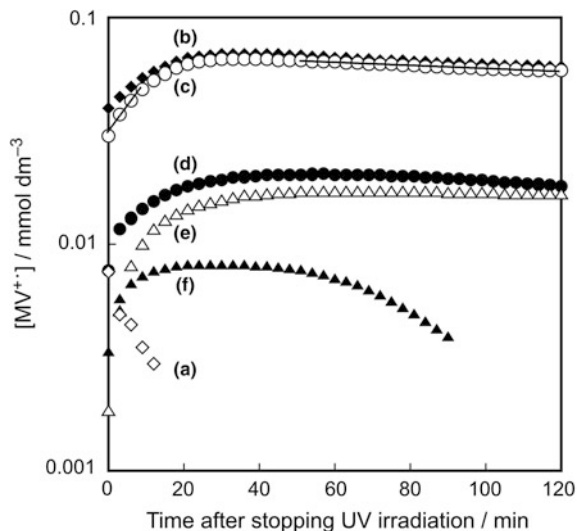
spatially separated functional moieties that are photocatalytically active niobate nanosheets and organic dye molecules on the clay nanosheets.

If an electron-accepting organic species (methyl viologen; MV^{2+}) is introduced to the niobate–clay colloids, photoinduced charge separation between the semi-conducting niobate and the acceptor selectively adsorbed on the clay occurs (Fig. 8.38) [208, 209]. The photochemical behavior is characterized by controllability of both the yield and stability of the photoproduct (MV^{+}) by the clay content. Figure 8.39 shows the amount of photoproduct in the colloids with various clay contents and their time-dependent decay after termination of the irradiation. The yield (maximum conversion) and lifetime of the product vary in the range of 8–70% and 10 min to 40 h, respectively, depending on the clay content, indicating that efficient and stable photoinduced charge separation is achieved under the optimum conditions.

On the other hand, the niobate–clay binary colloids exhibit photoinduced electron accumulation in the niobate nanosheets in the absence of an acceptor [224]. This process is also affected by the coexisting clay component, although the clay nanosheets do not directly contribute to the electron accumulation in the semi-conducting nanosheets. In contrast, the photochemical reaction is insensitive to the addition of molecular species that can work as electron donors; they somewhat destabilize the stable electron accumulation achieved by the addition of clay nanosheets. The results indicate that the photochemical reactions in the nanosheet colloid systems are not simply controlled by interactions between the semiconductor nanosheets and the additives at the molecular level but are governed by indirect interactions between the colloidal components.

Moreover, photocatalytic decomposition of a cationic dye has been studied in this binary colloid, where the dye is selectively adsorbed on the clay nanosheets to be spatially separated from the photocatalytic nanosheets [225]. Upon UV irradiation, the dye is photocatalytically decomposed in the colloids containing the niobate nanosheets, but self-photolysis of the dye is observed in the colloids lacking the photocatalytic nanosheets. In the binary colloid, the degradation is retarded

Fig. 8.39 Time courses of the concentration of MV^{2+} species observed after termination of UV irradiation in the MV/niobate–clay colloids with composition of [clay] = 1 (*a* open diamonds), 5 (*b* filled diamonds), 10 (*c* open circles), 20 (*d* filled circles), 25 (*e* open triangles), and 30 (*f* filled triangles) $g L^{-1}$, [niobate] = 1 $g L^{-1}$ and $[MV^{2+}] = 0.1 \text{ mmol } L^{-1}$. The lines overlapping with plot (*a*) indicate first-order kinetics obtained by fitting the plot. Reprinted with permission from [209]. Copyright 2009 American Chemical Society



compared with the single-component niobate colloid. A greater clay content better stabilized the dye against decomposition. In contrast, irradiation of the colloids with visible light caused self-photolysis of the dye, even in the presence of niobate nanosheets, indicating the absence of electron transfer from the photoexcited dye to the photocatalytic nanosheets.

8.7 Rheological Properties

A colloid dispersion of smectite-type clays, such as hectorite and montmorillonite, in water loses its fluidity above a concentration of several wt%. The rheological behavior of clay colloids changes depending on the shear and the time elapsed after colloid preparation. These behaviors are referred to as thixotropy. This interesting rheological behavior is important in view of the practical applications of colloid dispersion. In particular, clay minerals have been used in a wide variety of application fields, such as paints and cosmetics, as rheology modifiers. Hence, many research works have been carried out in view of the technical aspects to understand the phenomena of rheological behavior. However, the fundamental studies are not sufficient, and research to obtain rational models to explain the rheological behavior of colloid dispersions and the control of their properties based on the obtained model is underway. In this section, the rheology of nanosheet colloids is reviewed, particularly focusing on clay mineral systems.

8.7.1 Theory and Models

According to the classical theory, anisotropic colloidal particles have a much higher viscosity than spherical colloidal particles. In a flow field, solid colloidal particles cause perturbation to the fluidic flow and flow resistance, namely, a viscosity increase, compared with an isotropic solution. In a colloid dispersion, the following viscosity equation is formulated in a dilute particle concentration:

$$\eta_r = 1 + k\phi, \quad (8.14)$$

where η_r is the relative viscosity, ϕ is the volume fraction of particles (equal to the concentration), and k is a parameter. Whereas k is 2.5 for spherical colloidal particles (Einstein equation for viscosity), on anisotropic colloidal particles, there are several cases governed by both the orientations of the particles by flow and disorder of the orientation by the rotational Brownian motion, and these relationships make k larger than 2.5.

Additionally, the particle size of nanosheets influences the viscosity. The relationship between the intrinsic viscosity of polymer solution $[h]$ and molecular weight M is known as the Mark–Houwink–Sakurada equation, as follows:

$$[h] = kM^a,$$

where k and a are constants. Applying this empirical formula, it can be shown that a clay nanosheet colloid (two-dimensional inorganic polymer solution) with a larger particle size (molecular weight) has a higher viscosity.

However, the complex rheological behavior on clay colloids cannot be explained by the above-mentioned simple theories because, as described in Sect. 8.4, various attractive forces (electrostatic attraction, van der Waals force, hydrogen bonding, and depletion force), repulsive forces (electrostatic repulsion and steric repulsion), and other interactions (entropy-induced orientation and phase separation) are intertwined. The rational elucidation of the rheological behavior of clay colloids using these forces is not easy, and it has become a controversial issue. At the moment, there are two probable elucidations for the aggregation and resulting gelation of clay colloids: one is the “card-house” model, which assumes the attractive force between particles as the dominant factor, and the other is the “colloidal glass” model, which assumes the repulsive force as the dominant factor.

The “card-house” model is a classical model for the gelation of clay colloids proposed by van Olphen [226]. In this model, the gel formation of a clay colloid is explained by the formation of a macroscopic network structure, like a “house built of playing cards” (Fig. 8.40a), which is composed of T-shaped connections of the plane (mainly negatively charged) and edge (mainly positively charged) of the clay sheet through electrostatic attraction. In a Monte Carlo simulation study, a card-house structure appeared in a particle dispersion system with a negatively charged plane and a positively charged edge [227]. Whereas this model was widely regarded as a standard model, there are some questions about this extreme

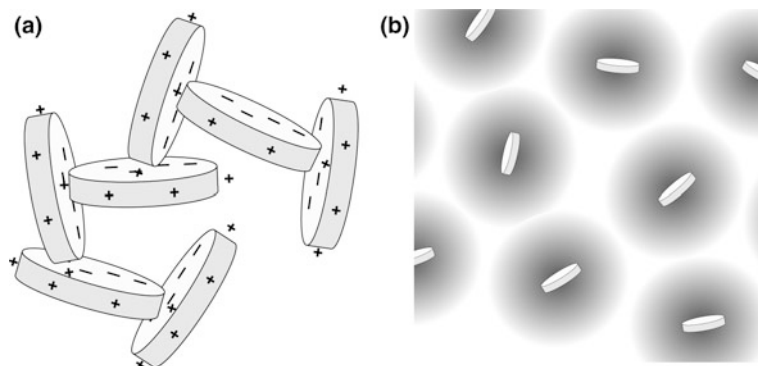
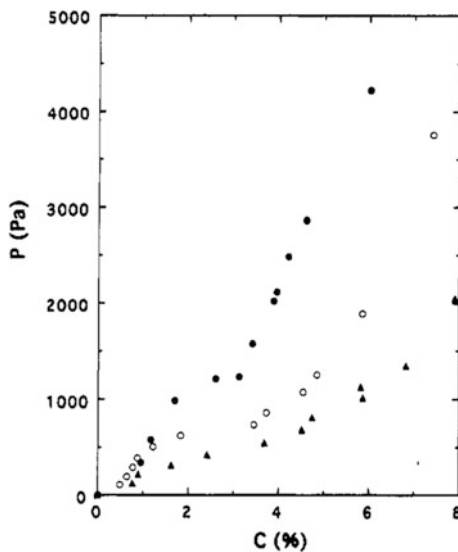


Fig. 8.40 Schematic illustration of the **a** house-of-cards structure and **b** colloidal glass of a clay nanosheet colloid

house-of-cards structure, and few experimental demonstrations of this structure formation have been reported. In a recent precise simulation [228], the card-house structure appeared only in the extremely restricted conditions. When the ionic strength is less than 5 mM, the interaction of the system is governed by only repulsive forces. When the ionic strength is greater than 5 mM, the overlapped state of the fringes of the clays becomes stable (such as the state of “layered coins”). When the ionic strength is greater than 100 mM, the van der Waals force becomes dominant, and the clay aggregates. In the first place, the AlOH and SiOH groups on the edge of the clay are charged only in the lower pH conditions in which AlOH^{2+} and SiOH^{2+} are generated by protonation. In the general conditions for clay colloids (pH = 12–13), AlOH and SiOH dissociate into negatively charged AlO^- and SiO^- , respectively. These dissociations are obvious from the zeta potential measurements [229]. On the other hand, much of the experimental evidence suggests that the macroscopic network structure is formed in clay colloids through the attractive interaction between nanosheets. [35, 37, 39, 40, 230–233]. It is probable that the formation of a network structure similar to “layered coins” originates from the attractive forces between nanosheets, such as the hydrogen bonding and van der Waals forces through the AlOH and SiOH groups on the edge of the clay, as well as the attractive electrostatic interaction mediated by the counterions.

The other model, the colloidal glass model (or Wigner glass model) explains the gelation of nanosheet colloids as the restricted motion of negatively charged nanosheets or their clusters caused by electrostatic repulsion among them [26, 39, 234–239], as illustrated in Fig. 8.40b. Mourchid [26, 39, 235] determined the phase diagrams of the sol-gel transition semiquantitatively by rheological measurements and tried to explain the colloidal glass model based on osmotic pressure measurements. They found that the osmotic pressure decreased with increasing ionic strength and remained positive regardless of the concentration of the colloid and the ionic strength (Fig. 8.41). These results can be explained by the shielding of the electrostatic repulsion between particles due to the increased ionic strength and

Fig. 8.41 Equations of state of the Laponite suspensions as a function of the ionic strength I : (filled circle) $I = 10^{-4}$ M, (open circle) $I = 5 \times 10^{-3}$ M, and (filled triangle) $I = 5 \times 10^{-2}$ M. Reprinted with permission from Ref. [39]. Copyright 1995 American Chemical Society



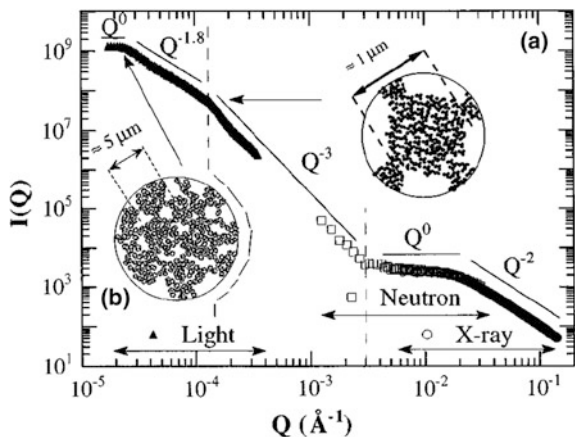
indicate that repulsive interaction was dominant in the system. The model is also supported by the phenomenon that the viscosity of the clay colloidal sol was decreased by adding a small quantity of salt [240–242] and the phenomenon that the onset concentration of the sol-gel transition increased with increasing ionic strength [243]. Michot et al. recently investigated the nontronite and montmorillonite systems and reported that the change of rheology by the colloid concentration, particle size, and ionic strength could be explained by the repulsive force only model [24, 25, 48]. However, as shown in the next section, the existence of a network structure in the gel was suggested by the structural analyses based on the results of the small-angle scattering [35, 37, 39, 40, 230–233]. These results contradict the colloid glass model.

8.7.2 Colloid Structure and Rheology

To clarify the gelation mechanism of nanosheet colloids, discussion of the colloid structure is very important. Whereas the formation of the anisotropic structure of the clay colloid in the liquid crystal state was described in the former section, detailed structural analyses by small-angle scattering methods (light, X-ray, and neutrons) have been carried out also for isotropic and gel phase clay colloids, and the relationship between the structure and its rheological behavior was discussed [35, 37–40, 244].

In small-angle scattering measurement of a dilute Laponite colloid, such as ca. 1%, the scattering curve almost coincided with the theoretical scattering curve for disc-like particles with 25 nm diameter and 1 nm thickness [36, 245–248]. In the region of the smaller scattering vector q , namely, the region that reflects the larger

Fig. 8.42 Small-angle X-ray and neutron scattering and static light scattering from an aqueous Laponite suspension at rest, at volume fraction 1.6%, ionic strength of 1×10^3 M, pH 9.5, and stored for 200 days. *a* Dense micrometer-sized aggregates and *b* mass fractal made of alternating aggregates and voids. Reprinted with permission from the reference [38]. Copyright 2002 American Physical Society



structure, excess scattering is sometimes observed, suggesting that the distribution of colloidal particles is not uniform. For example, Fig. 8.42 shows the results of the small-angle scattering of a Laponite colloid reported by Pignon et al. [37, 38]. The power laws of q^{-3} and $q^{-1.8}$ are observed. In general, a scattering curve with a power law of q^{-D} is ascribed to a mass fractal structure with fractal dimension D . Similar scattering results were reported by several other groups. These results were, regardless of the true structure, ascribed to an inhomogeneous structure with fractal dimension of 2–3, and some estimated structures, such as that shown in Fig. 8.43, were demonstrated.

Furthermore, Pignon et al. revealed that the power law of the SAXS pattern of the Laponite colloid changes from q^{-1} to $q^{-1.8}$ when increasing the concentration and ionic strength and as the gelation proceeds. The change of the fractal dimension (corresponding to the network structure) corresponded to a change of the yield stress so that it was concluded that the formation of a macroscopic inhomogeneous structure with up to micrometer scale dominated the rheological properties. However, the results of the small-angle scattering, ascribable to the fractal structure, were also observed in the niobate nanosheet system, showing an extremely lower viscosity compared to clay minerals [34]. Therefore, careful consideration is required to discuss the direct relationship between the structure and the high viscosity of the nanosheet colloid.

The structural changes of the colloid induced by shear [245] or with time [230, 249–256] were studied in detail, and important results to discuss the thixotropic behavior and gelation mechanism of the nanosheet colloids were obtained. Bonn and Tanaka obtained the phase diagram shown in Fig. 8.44 based on the time-course results of dynamic and static light scattering on a Laponite colloid system [239, 250, 254–256]. They claim that “clay colloids with no fluidity” can be classified as two different states, “gel” or “glass,” depending on the conditions. They define “gel” as a network structure formed by dominant attractive forces, such as van der Waals force, in the region where the electrostatic repulsion force is

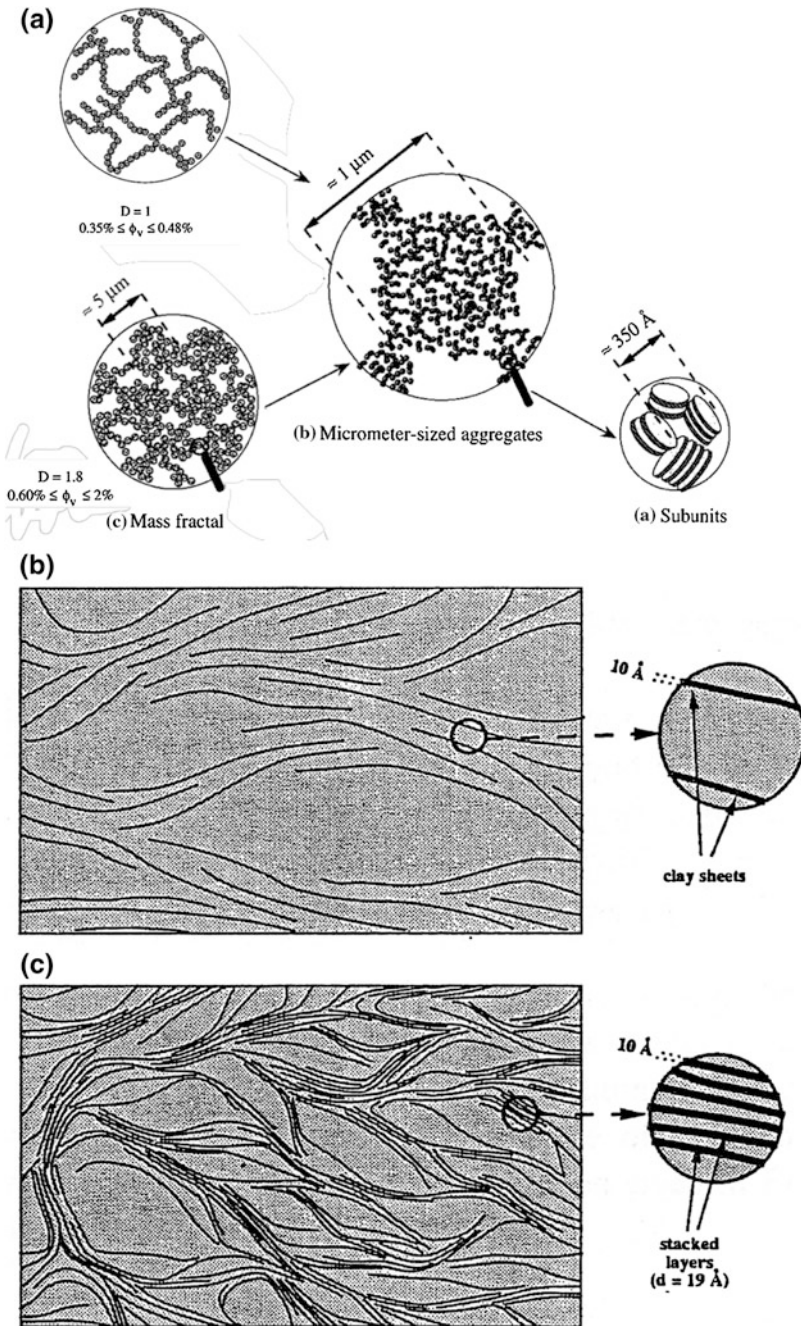
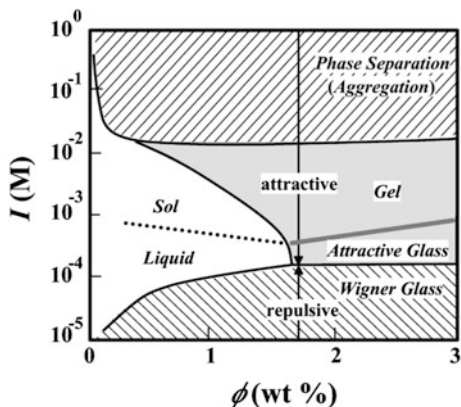


Fig. 8.43 Schematic illustrations of the fractal structure of the clay colloids presented by a Pignon [38] and b, c Morvan [40]. Reprinted with permission from the publishers. Copyright 1997 American Physical Society. Copyright 1994 Elsevier

Fig. 8.44 Phase diagram of Laponite suspensions. Coexistence of phase separation and gelation is characteristic of a system that forms “physical” gel. Strictly speaking, this should be called a state diagram since a system is not in an equilibrium state. Reprinted with permission from Ref. [250]. Copyright 2002 American Physical Society

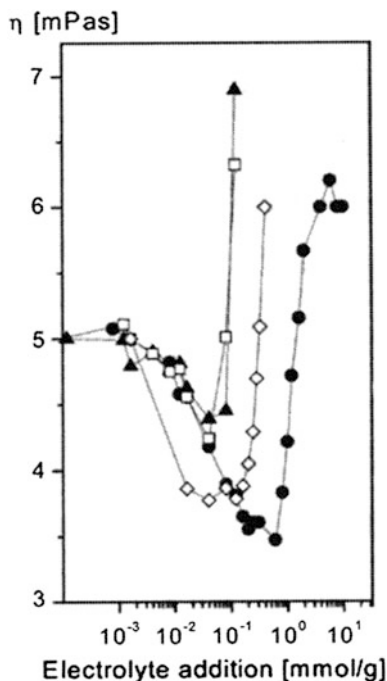


shielded at relatively high ionic strength. In this region, the growth of inhomogeneous clusters or network structures was observed with time. “Wigner glass” (repulsive colloidal glass) is a typical colloidal glass that emerges when the electrostatic repulsive force is dominant in a lower salt concentration and when the sum of effective volume of colloid particles, including the Debye length, exceeds the volume of the system. In this type, the structure showed homogeneity and did not change with time. The motility of the particles was typical to colloidal glasses and was maintained with vibration in a small region, even after aging. The other phase, “attractive colloidal glass” appears in the intermediate region between the “gel” and the “Wigner glass.” This phase is composed of nanosheet clusters, not individual nanosheets, as the unit particle, so that an inhomogeneous structure grows with time and the particles show no motility after aging.

8.7.3 Control of the Rheological Properties of the Nanosheet Colloids

In this final chapter, the reports on controlling the rheological properties of nanosheet colloids are presented. Largely et al. investigated the viscosity change of montmorillonite colloid after adding various types of salts and acids [240–242]. Figure 8.45 shows the viscosity change of montmorillonite colloids with the addition of various salts. Whereas the addition of a small quantity of salt decreased the viscosity due to shielding of the electrostatic repulsion between nanosheet colloids, a large quantity of salt caused an abrupt increase in the viscosity due to attractive interaction between nanosheets and the formation of an aggregated structure, named as an attractive gel. The viscosity depended on the species of salt. When a small amount of phosphate or pyrophosphate was added to the clay colloid,

Fig. 8.45 Viscosity η at a shear rate of 120 s^{-1} for the 2% sodium montmorillonite dispersion in the presence of *filled circle* NaCl, *open diamond* NaNO_3 , *filled triangle* HCl, and *open square* HNO_3 . Reprinted with permission from Ref. [241]. Copyright 2001 Elsevier

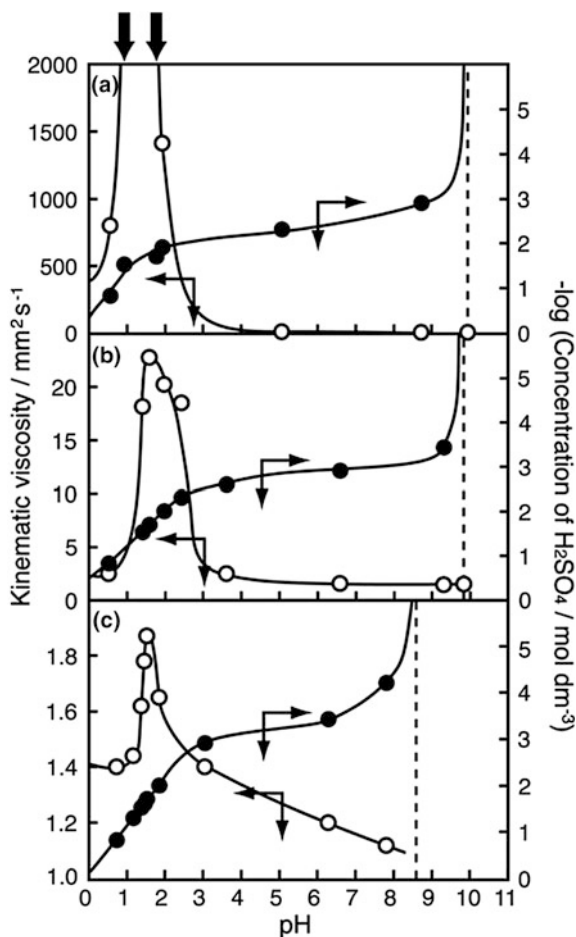


the viscosity decreased greatly [241, 242]. The addition of polyelectrolytes, such as sodium polyacrylate [257], and nonionic polymers, such as poly(ethylene oxide), was also examined. In these cases, the viscosity decreased with the addition of a lower molecular weight polymer, whereas it increased with addition of a higher molecular weight polymer.

We found a pH-induced gelation of an exfoliated nanosheet colloid of layered niobate $\text{K}_4\text{Nb}_6\text{O}_{17}$ [258, 259]. When HCl or H_2SO_4 was added to the colloid ($\sim 10 \text{ gL}^{-1}$) and the pH was adjusted to 1.5, a physical gel was formed. Figure 8.46 shows the appearance of the colloid in the gel state. The change of pH changed the surface charge of the niobate nanosheet and influenced the electrostatic interaction between nanosheets. This process coincides with the gelation process of the clay colloid.

The lateral size of the nanosheet is also considered an important factor to control the viscosity. In the hexaniobate nanosheet system with controlled lateral size, colloids of the nanosheets with larger lateral size had higher viscosity [17]. However, in clay mineral systems, the opposite trend was reported for montmorillonite [25] and nontronite [24, 48]. Laponite, a synthetic hectorite with very small particle size of 25 nm [236], shows an extraordinarily high viscosity at low concentration. Thus we can not find any general trend for the relationship between the lateral size and the viscosity. Further systematic investigations are needed to understand the effect of nanosheet size on the viscosity.

Fig. 8.46 Variations in kinematic viscosity of the niobate nanosheet colloids with pH (open circles), and titration curves of the colloids (relationship between pH and concentration of H_2SO_4 added) (filled circles). The colloids contain **a** 7.3, **b** 2.4, and **c** 0.8 g dm^{-3} of $[\text{Nb}_6\text{O}_{17}]^{4-}$, respectively. For the colloid containing 7.3 g dm^{-3} of $[\text{Nb}_6\text{O}_{17}]^{4-}$, viscosity was too high to be measured at pHs indicated by the arrows on the top. The dashed lines show pHs where $[\text{SO}_4^{2-}] \sim 0$. Reprinted with permission from the reference [258]. Copyright 2002 The Royal Society of Chemistry



8.8 Summary and Outlook

The fundamentals and applications of colloidal nanosheets were reviewed. Liquid crystal phases of nanosheet colloids and control of them by external field are emerging as important topics because the intriguing hierarchical structure of the nanosheet can be assembled. Although we still have fundamental issues such as control of stability and rheological property and understanding of the structure formation mechanisms, some of novel colloidal materials and composite materials were successfully reported already. Further development of the researches on colloidal nanosheets will lead to many applications such as optical and electronic devices, medical materials, composite materials with good mechanical and barrier properties, structural colors materials for sensors and cosmetics, and composite gels for soft actuators.

Acknowledgements A part of this work was supported by Research Center for Materials and Energy Devices of Fukuoka Institute of Technology (FIT-ME) (Strategic Research Foundation Grant-Aided Project for Private University from MEXT) as well as by Canon Foundation, KAKENHI (#24104005 and #15K05657), and Network Joint Research Center for Materials and Devices (#201507 and #20166009).

References

1. Verwey EJW, Overbeek JTG (1948) Theory of the stability of lyophobic colloids. Elsevier, Amsterdam
2. Smalley M (2006) Clay swelling and colloid stability. CRC Press, New York
3. Livolant F, Levelut AM, Doucet J, Benoit JP (1989) Nature 339:724
4. Strzelecka TE, Davidson MW, Rill RL (1988) Nature 331:457
5. Sato T, Teramoto A (1996) Adv Polymer Sci 126:85
6. Bawden FC, Pirie NW, Bernal JD, Fankuchen I (1936) Nature 138:1051
7. Jana NR, Gearheart LA, Obare SO, Johnson CJ, Edler KJ, Mann S, Murphy CJ (2002) J Mater Chem 12:2909
8. Kajiwara K, Donkai N, Hiragi Y, Inagaki H (1986) Makromol Chem 187:2883
9. van Bruggen MPB, van der Kooij FM, Lekkerkerker HNW (1996) J Phys: Condens Matter 8:9451
10. Lemaire BJ, Panine P, Gabriel JCP, Davidson P (2002) Europhys Lett 69:55
11. Li L, Walda J, Manna L, Alivisatos AP (2002) Nano Lett 2:557
12. van der Kooij FM, Kassapidou K, Lekkerkerker HNW (2000) Nature 406:868
13. van der Kooij FM, Lekkerkerker HNW (1998) J Phys Chem B 102:7829
14. Brown ABD, Ferrero C, Narayanan T, Rennie AR (1999) Eur Phys J B 11:481
15. Liu S, Zhang J, Wang N, Liu W, Zhang C, Sun D (2003) Chem Mater 15:3240
16. Gabriel J-CP, Camerel F, Lemaire BJ, Desvaux H, Davidson P, Batail P (2001) Nature 413:504
17. Miyamoto N, Nakato T (2004) J Phys Chem B 108:6152
18. Nakato T, Miyamoto N, Harada A (2004) Chem Commun 78
19. Nakato T, Yamashita Y, Kuroda K (2006) Thin Solid Films 495:24
20. Miyamoto N, Yamamoto S, Shimasaki K, Harada K, Yamauchi Y (2011) Chem Asian J 6:2936
21. Xu Z, Gao C (2011) ACS Nano 5:2908
22. Miyamoto N, Iijima H, Ohkubo H, Yamauchi Y (2010) Chem Commun 46:4166
23. Paineau E, Antonova K, Baravian C, Bihannic I, Davidson P, Dozov I, Impéror-Clerc M, Levitz P, Madsen A, Meneau F, Michot LJ (2009) J Phys Chem B 113:15858
24. Michot LJ, Bihannic I, Maddi S, Baravian C, Levitz P, Davidson P (2008) Langmuir 24:3127
25. Michot LJ, Bihannic I, Porsch K, Maddi S, Baravian C, Mougel J, Levitz P (2004) Langmuir 20:10829
26. Mourchid A, Lécolier E, van Damme H, Levitz P (1998) Langmuir 14:4718
27. Onsager L (1949) Ann NY Acad Sci 51:627
28. Mejia AF, Chang Y-W, Ng R, Shuai M, Mannan MS, Cheng Z (2012) Phys Rev E 85:061708
29. Wong M, Ishige R, Hoshino T, Hawkins S, Li P, Takahara A, Sue H-J (2014) Chem Mater 26:1528
30. Miyamoto N, Nakato T (2002) Adv Mater 14:1267
31. Miyamoto N, Kuroda K, Ogawa M (2004) J Phys Chem B 108:4268
32. Miyamoto N, Yamamoto H, Kaito R, Kuroda K (2002) Chem Commun 2378

33. Yamaguchi D, Miyamoto N, Fujita T, Nakato T, Koizumi S, Ohta N, Yagi N, Hashimoto T (2012) *Phys Rev E* 85:011403
34. Yamaguchi D, Miyamoto N, Koizumi S, Nakato T, Hashimoto T (2007) *J Appl Cryst* 40: s101
35. Bhatia S, Barker J, Mourchid A (2003) *Langmuir* 19:532
36. Kroon M, Vos WL, Wegdam GH (1998) *Phys Rev E* 57:1962
37. Pignon F, Magnin A, Piau J-M (1997) *Phys Rev Lett* 4689:4689
38. Pignon F, Magnin A, Piau J-M, Cabane B, Lindner P, Diat O (1997) *Phys Rev E* 56:3281
39. Mourchid A, Delville A, Lambard J, Lécolier E, Levitz P (1995) *Langmuir* 11:1942
40. Morvan M, Espinat D, Lambard J, Zemb T (1994) *Colloids Surf A* 82:193
41. Treacy MMJ, Rice SB, Jacobson AJ, Lewandowski JT (1990) *Chem Mater* 2:279
42. Ebina Y, Sasaki T, Harada M, Watanabe M (2002) *Chem Mater* 14:4390
43. Takagaki A, Sugisawa M, Lu D, Kondo JN, Hara M, Domen K, Hayashi S (2003) *J Am Chem Soc* 125:5479
44. Kudo A, Sakata T (1995) *J Phys Chem* 99:15963
45. *Langmuir* I (1938) *J Chem Phys* 6:873
46. Gabriel J-CP, Sanchez C, Davidson P (1996) *J Phys Chem* 100:11139
47. DiMasi E, Fossum JO, Gog T, Venkataraman C (2001) *Phys Rev E* 64:061704
48. Michot LJ, Baravian C, Bihannic I, Maddi S, Moynes C, Duval JFL, Levitz P, Davidson P (2009) *Langmuir* 25:127
49. Michot LJ, Bihannic I, Maddi S, Funari SS, Baravian C, Levitz P, Davidson P (2006) *Proc Nat Acad Sci* 103:16101
50. Paineau E, Michot LJ, Bihannic I, Baravian C (2011) *Langmuir* 27:7806
51. Paineau E, Bihannic I, Baravian C, Philippe A-M, Davidson P, Levitz P, Funari S, Rochas C, Michot LJ (2011) *Langmuir* 27:5562
52. Baravian C, Michot LJ, Paineau E, Bihannic I, Davidson P, 'ror-Clerc MI, Belamie E, Levitz P (2010) *Europhys Lett* 60:36005
53. Hemmen H, Ringdal NI, Azevedo END, Engelsberg M, Hansen EL, Meheust Y, Fossum JO, Knudsen KD (2009) *Langmuir* 25:12507
54. Dan B, Behabtu N, Martinez A, Evans JS, Kosynkin DV, Tour JM, Pasquali M, Smalyukh II (2011) *Soft Matter* 7:11154
55. Kim JE, Han TH, Lee SH, Kim JY, Ahn CW, Yun JM, Kim SO (2011) *Angew Chem Int Ed* 50:3043
56. Aboutalebi SH, Gudarzi MM, Zheng QB, Kim J-K (2011) *Adv Funct Mater* 21:2978
57. Xu Z, Gao C (2011) *Nat Commun* 2:571
58. Zocher VH (1925) *Anorg Allg Chem* 147:91
59. Davidson P, Garreau A, Livage J (1994) *Liq Cryst* 16:905
60. Davidson P, Bourgaux C, Schoutteten L, Sergot P, Williams C, Livage J (1995) *J Phys II France* 5:1577
61. Pelletier O, Bourgaux C, Diat O, Davidson P, Livage J (1999) *Eur Phys J B* 12:541
62. Lamarque-Forget S, Pelletier O, Dozov I, Davidson P, Martinot-Lagarde P, Livage J (2000) *Adv Mater* 12:1267
63. Desvaux H, Gabriel J-CP, Berthault P, Camerel F (2001) *Angew Chem Int Ed* 40:373
64. Commeinhes X, Davidson P, Bourgaux C, Livage J (1997) *Adv Mater* 9:900
65. Adachi-Pagano M, Forano C, Besse J-P (2000) *Chem Commun* 91
66. Hibino T, Jones WJ (2001) *J Mater Chem* 11:1321
67. Iyi N, Ebina Y, Sasaki T (2008) *Langmuir* 24:5591
68. Iyi N, Ebina Y, Sasaki T (2011) *J Mater Chem* 21:8085
69. Wang N, Liu S, Zhang J, Wu Z, Chenb J, Sun D (2005) *Soft Matter* 1:428
70. Zhang J, Luan L, Zhu W, Liu S, Sun D (2007) *Langmuir* 23:5331
71. Mourad MCD, Devid EJ, Schooneveld MMv, Vonk C, Lekkerkerker HNW (2008) *J Phys Chem B* 112:10142
72. Zhu W, Sun D, Liu S, Wang N, Zhang J, Luan L (2007) *Colloids Surf A* 301:106
73. Luan L, Liu S, Sun D (2009) *J Solid State Chem* 182:1462

74. Luan L, Li W, Liu S, Sun D (2009) *Langmuir* 25:6349
75. Shen T-Z, Hong S-H, Song J-K (2014) *Nature Mater* 13:394
76. Brown ABD, Clarke SM, Rennie AR (1998) *Langmuir* 14:3192
77. Bates M, Frenkel D (1999) *J Chem Phys* 110:6553
78. Ise N, Sogami IS (2005) *Structure formation in solution—ionic polymers and colloidal particles*. Springer, Berlin
79. Geng F, Ma R, Nakamura A, Akatsuka K, Ebina Y, Yamauchi Y, Miyamoto N, Tateyama Y, Sasaki T (2013) *Nat Commun* 4:1632
80. Geng F, Ma R, Ebina Y, Yamauchi Y, Miyamoto N, Sasaki T (2014) *J Am Chem Soc* 136:5491
81. Song Y, Iyi N, Hoshide T, Ozawa TC, Ebina Y, Ma R, Miyamoto N, Sasaki T (2015) *Chem Commun* 51:17068
82. Helfrich W (1978) *Naturforsch* 33a:305
83. Kunz DA, Feicht P, Godrich S, Thurn H, Papastavrou G, Fery A, Breu J (2013) *Adv Mater* 25:1337
84. Marshall CE (1930) *Trans Faraday Soc* 26:173
85. Mueller H (1939) *Phys Rev* 55:508
86. Mueller H (1939) *Phys Rev* 55:792
87. Sugimoto W, Terabayashi O, Murakami Y, Takatsu Y (2002) *J Mater Chem* 12:3814
88. Nakato T, Nakamura K, Shimada Y, Shido Y, Houryu T, Iimura Y, Miyata H (2011) *J Phys Chem C* 115:8934
89. Shah MJ (1963) *J Phys Chem* 67:2215
90. Yamaoka K, Sasai R, Ikuta N (1994) *Chem Lett* 563
91. Sasai R, Yamaoka K (1995) *J Phys Chem* 99:17754
92. Shah MJ, Thompson DC, Hart CM (1963) *J Phys Chem* 67:1170
93. Yamaoka K, Tanigawa M, Sasai R (1994) *J Chem Phys* 101:1625
94. Sasai R, Ikuta N, Yamaoka K (1996) *J Phys Chem* 100:17266
95. Holzheu S, Hoffmann H (2002) *J Phys Chem B* 106:4412
96. O'Konski CT, Bergmann K (1962) *J Chem Phys* 37:1573
97. Yamagishi A, Soma M (1981) *J Phys Chem* 85:3090
98. Yamagishi A, Taniguchi M, Takahashi M, Asada C, Matsushita N, Sato H (1994) *J Phys Chem* 98:7555
99. Yamaoka K, Sasai R, Takata N (2000) *Colloids Surf A* 175:23
100. Yamaoka K, Sasai R (2000) *J Colloid Interface Sci* 225:82
101. Yamagishi A (1982) *Inorg Chem* 21:1778
102. Winslow WM (1949) *J Appl Phys* 20:1137
103. Dürschmidt T, Hoffmann H (1999) *Colloids Surf A* 156:257
104. Kim JW, Kim SG, Choi HJ, Jhon MS (1999) *Macromol Rapid Comm* 20:450
105. Lu J, Zhao XP (2002) *J Mater Chem* 12:2603
106. Fossum JO, Méheust Y, Parmar KPS, Knudsen KD, Måløy KJ, Fonseca DM (2006) *Europhys Lett* 74:438
107. Zhang WL, Liu YD, Choi HJ (2011) *J Mater Chem* 21:6916
108. Xiang LQ, Zhao XP (2003) *J Mater Chem* 13:1529
109. Kim YJ, Liu YD, Choi HJ, Park S-J (2013) *J Colloid Interface Sci* 394:108
110. Zhang WL, Choi HJ (2011) *Chem Commun* 47:12286
111. Yin J, Wang X, Chang R, Zhao X (2012) *Soft Matter* 8:294
112. Yin J, Chang R, Kai Y, Zhao X (2013) *Soft Matter* 9:3910
113. Parmar KPS, Meheust Y, Schjelderupsen B, Fossum JO (2008) *Langmuir* 24:1814
114. Shin KY, Lee S, Hong S, Jang J (2014) *ACS Appl Mater Interfaces* 6:5531
115. Kimura H, Sugiyama T, Takahashi S, Tsuchida A (2013) *Rheol Acta* 52:139
116. Kimura H, Ueno M, Takahashi S, Tsuchida A, Kurosaka K (2014) *Appl Clay Sci* 99:160
117. Kimura H, Nakashima A, Takahashi S, Tsuchida A, Kurosaka K (2015) *Appl Clay Sci* 114:120

118. Dozov I, Paineau E, Davidson P, Antonova K, Baravian C, Bihannic I, Michot LJ (2011) *J Phys Chem B* 115:7751
119. Hong S-H, Shen T-Z, Song J-K (2014) *J Phys Chem C* 118:26304
120. Porion P, Faugere AM, Michot LJ, Paineau E, Delville A (2011) *J Phys Chem C* 115:14253
121. Eguchi M, Angelone MS, Yennawar HP, Mallouk TE (2008) *J Phys Chem C* 112:11280
122. Wu LL, Ohtani M, Takata M, Saeki A, Seki S, Ishida Y, Aida T (2014) *ACS Nano* 8:4640
123. Azevedo ENd, Engelsberg M, Fossum JO, Souza REd (2007) *Langmuir* 23:5100
124. Osterloh FE (2002) *J Am Chem Soc* 124:6248
125. Kim JY, Osterloh FE, Hiramatsu H, Dumas RK, Liu K (2005) *J Phys Chem B* 109:11151
126. Beydaghi H, Javanbakht M (2015) *Ind Eng Chem Res* 54:7028
127. Guo F, Kim F, Han TH, Shenoy VB, Huang J, Hurt RH (2011) *ACS Nano* 5:8019
128. Liu Z, Li Z, Xu Z, Xia Z, Hu X, Kou L, Peng L, Wei Y, Gao C (2014) *Chem Mater* 26:6786
129. Takagi S, Shimada T, Eguchi M, Yui T, Yoshida H, Tryk DA, Inoue H (2002) *Langmuir* 18:2265
130. Kawamata J, Suzuki Y, Tenma Y (2010) *Phil Mag* 90:2519
131. Miyamoto N, Kuroda K, Ogawa M (2004) *J Mater Chem* 14:165
132. Jalili R, Aboutalebi SH, Esrafilzadeh D, Konstantinov K, Moulton SE, Razal JM, Wallace GG (2013) *ACS Nano* 7:3981
133. Yang X, Qiu L, Cheng C, Wu Y, Ma ZF, Li D (2011) *Angew Chem Int Ed* 50:7325
134. Jalili R, Aboutalebi SH, Esrafilzadeh D, Shepherd RL, Chen J, Aminorroaya-Yamini S, Konstantinov K, Minett AI, Razal JM, Wallace GG (2013) *Adv Funct Mater* 23:5345
135. Seyedin MZ, Razal JM, Innis PC, Jalili R, Wallace GG (2015) *Adv Funct Mater* 25:94
136. Kim YS, Kang JH, Kim T, Jung Y, Lee K, Oh JY, Park J, Park CR (2014) *Chem Mater* 26:5549
137. Nakato T, Nono Y, Mouri E, Nakata M (2014) *Phys Chem Chem Phys* 16:955
138. Yamaki T, Asai K (2001) *Langmuir* 17:2564
139. Umemura Y, Yamagishi A, Schoonheydt R, Persoons A, Schryver FD (2002) *J Am Chem Soc* 124:992
140. Inukai K, Hotta Y, Taniguchi M, Tomura S, Yamagishi A (1994) *J Chem Soc Chem Commun* 959
141. Binks BP (2002) *Curr Opin Colloid Inter Sci* 7:21
142. Binks BP, Horozov TS (2006) *Colloidal particles at liquid interfaces*. Cambridge University Press, Cambridge
143. Aveyard R, Binks BP, Clint JH (2003) *Adv Colloid Interface Sci* 100–102:503
144. Fujii S, Murakami R (2008) *KONA Powder Technol J* 26:153
145. Nonomura Y, Kobayashi N (2009) *J Colloid Inter Sci* 330:463
146. Booth SG, Dryfe RAW (2015) *J Phys Chem C* 119:23295
147. Mejia AF, Diaz A, Pullela S, Chang Y-W, Simonetty M, Carpenter C, Batteas JD, Mannan MS, Clearfield A, Cheng Z (2012) *Soft Matter* 8:10245
148. Tsugita A, Takemoto S, Mori K, Yoneya T, Otani Y (1983) *J Colloid Inter Sci* 95:551
149. Ashby NP, Binks BP (2000) *Phys Chem Chem Phys* 2:5640
150. Abend S, Bonnke N, Gutschner U, Lagaly G (1998) *Colloid Polym Sci* 276:730
151. Bolhuis P, Frenkel D (1994) *J Chem Phys* 101:9869
152. Yang F, Liu S, Xu J, Lan Q, Wei F, Sun D (2006) *J Colloid Inter Sci* 302:159
153. Hirsemann D, Shylesh S, De Souza RA, Diar-Bakerly B, Biersack B, Mueller DN, Martin M, Schobert R, Breu J (2012) *Angew Chem Int Ed* 51:1348
154. Nakato T, Ueda H, Hashimoto S, Terao R, Kameyama M, Mouri E (2012) *ACS Appl Mater Interfaces* 4:4338
155. Dong J, Worthen AJ, Foster LM, Chen Y, Cornell KA, Bryant SL, Truskett TM, Bielawski CW, Johnston KP (2014) *ACS Appl Mater Inter* 6:11502
156. Zhang S, Sun D, Dong X, Li C, Xu J (2008) *Colloids Surf A* 324:1
157. Liu Q, Luan L, Sun D, Xu J (2010) *J Colloid Interface Sci* 343:87
158. Tran DN, Whitby CP, Fornasiero D, Ralston J (2010) *J Colloid Interface Sci* 348:460
159. Binks BP, Sekine T, Tyowua AT (2014) *Soft Matter* 10:578

160. He Y, Wu F, Sun X, Li R, Guo Y, Li C, Zhang L, Xing F, Wang W, Gao J (2013) *ACS Appl Mater Interfaces* 5:4843
161. McCoy TM, Pottage MJ, Tabor RF (2014) *J Phys Chem C* 118:4529
162. Kim J, Cote LJ, Kim F, Yuan W, Shull KR, Huang J (2010) *J Am Chem Soc* 132:8180
163. Gudarzi MM, Sharif F (2011) *Soft Matter* 7:3432
164. Guevara JS, Mejia AF, Shuai M, Chang Y-W, Mannan MS, Cheng Z (2013) *Soft Matter* 9:1327
165. Haraguchi K, Li H-J, SOng L, Murata K (2007) *Macromolecules* 40:6973
166. Ma X, Li Y, Wang W, Ji Q, Xi Y (2013) *Eur Polymer J* 49:389
167. Liu M, Ishida Y, Ebina Y, Sasaki T, Aida T (2013) *Nat Commun* 4:2029
168. Liu J, Song G, He C, Wang H (2013) *Macromol Rapid Commun* 34:1002–1007
169. Fan J, Shi Z, Lian M, Li H, Yin J (2013) *J Mater Chem A* 1:7433
170. Shen J, Yan B, Li T, Long Y, Li N, Ye M (2012) *Soft Matter* 8:1831
171. Haraguchi K, Takada T (2010) *Macromolecules* 43:4294
172. Paineau E, Dozov I, Bihannic I, Baravian C, Krapf M-EM, Philippe A-M, Rouziere SAH, Michot LJ, Davidson P (2012) *ACS Appl Mater Interfaces* 4:4296
173. Inadomi T, Ikeda S, Okumura Y, Kikuchi H, Miyamoto N (2014) *Macromol Rapid Commun* 35:1741
174. Miyamoto N, Shintate M, Ikeda S, Hoshida Y, Yamauchi Y, Motokawa R, Annaka M (2013) *Chem Commun* 49:1082
175. Mejia AF, Ng R, Nguyen P, Shuai M, Acosta HY, Mannan MS, Cheng Z (2013) *Soft Matter* 9:10257
176. Liu M, Ishida Y, Ebina Y, Sasaki T, Hikima T, Takata M, Aida T (2015) *Nature* 517:68
177. Kim YS, Liu M, Ishida Y, Ebina Y, Osada M, Sasaki T, Hikima T, Takata M, Aida T (2015) *Nat Mater* 14:1002
178. Adams M, Dogic Z, Keller SL, Fraden S (1998) *Nature* 393:349
179. van der Kooij FM, Lekkerkerker HNW (2000) *Phys Rev Lett* 84:781
180. Oversteegen SM, Wijnhoven JGEJ, Vonk C, Lekkerkerker HNW (2004) *J Phys Chem B* 108:18158
181. Dogic Z, Purdy K, Grelet E, Adams M, Fraden S (2004) *Phys Rev E* 69:051702
182. Moulton SE, Maugey M, Poulin P, Wallace GG (2007) *J Am Chem Soc* 129:9452
183. Yasarawan N, van Duijneveldt JS (2010) *Soft Matter* 6:353
184. Kleshchanok D, Petukhov AV, Holmqvist P, Byelov DV, Lekkerkerker HN (2010) *Langmuir* 26:13614
185. Doshi N, Cinacchi G, van Duijneveldt JS, Cosgrove T, Prescott SW, Grillo I, Phipps J, Gittins DI (2011) *J Phys: Condens Matter* 23:194109
186. Kleshchanok D, Meijer J-M, Petukhov AV, Portale G, Lekkerkerker HNW (2012) *Soft Matter* 8:191
187. Kleshchanok D, Meester V, Pompe CE, Hilhorst J, Lekkerkerker HN (2012) *J Phys Chem B* 116:9532
188. Zhang J, Lang PR, Meyer M, Dhont JKG (2013) *Langmuir* 29:4679
189. Harnau L (2008) *Mol Phys* 106:1975
190. Stroobants A, Lekkerkerker HNW (1984) *J Phys Chem* 88:3669
191. Bates MA, Frenkel D (2000) *Phys Rev E* 62:5225
192. Varga S, Galindo A, Jackson G (2002) *J Chem Phys* 117:7207
193. Camp PJ, Allen MP (1996) *Phys A* 229:410
194. Varga S, Galindo A, Jackson G (2002) *Phys Rev E* 66:011707
195. Oversteegen SM, Lekkerkerker HN (2004) *J Chem Phys* 120:2470
196. Harnau L, Dietrich S (2004) *Phys Rev E* 69:051501
197. Harnau L, Dietrich S (2002) *Phys Rev E Stat Nonlin Soft Matter Phys* 66:051702
198. Bier M, Harnau L, Dietrich S (2005) *J Chem Phys* 123 No. 114906
199. Phillips J, Schmidt M (2010) *Phys Rev E* 81:041401
200. Verhoeff AA, Wensink HH, Vis M, Jackson G, Lekkerkerker HNW (2009) *J Phys Chem B* 113:13476

201. van der Kooij FM, Lekkerkerker HNW (2000) *Langmuir* 16:10144
202. van der Kooij FM, Vogel M, Lekkerkerker HNW (2000) *Phys Rev E* 62:5397
203. Chen M, Li H, Chen Y, Mejia AF, Wang X, Cheng Z (2015) *Soft Matter* 11:5775
204. Landman J, Paineau E, Davidson P, Bihannic I, Michot LJ, Philippe AM, Petukhov AV, Lekkerkerker HN (2014) *J Phys Chem B* 118:4913
205. Cousin F, Cabuil V, Grillo I, Levitz P (2008) *Langmuir* 24:11422
206. Woolston P, van Duijneveldt JS (2015) *Langmuir* 31:9290
207. Miyamoto N, Nakato T (2003) *Langmuir* 19:8057
208. Miyamoto N, Yamada Y, Koizumi S, Nakato T (2007) *Angew Chem Int Ed* 46:4123
209. Nakato T, Yamada Y, Miyamoto N (2009) *J Phys Chem B* 113:1323
210. Nakato T, Yamashita Y, Mouri E, Kuroda K (2014) *Soft Matter* 10:3161
211. Pujala RK, Pawar N, Bohidar HB (2011) *Langmuir* 27:5193
212. Pujala RK, Bohidar HB (2012) *Soft Matter* 8:6120
213. Zhang C, Tjui WW, Fan W, Yang Z, Huang S, Liu T (2011) *J Mater Chem* 21:18011
214. Fang B, Peng L, Xu Z, Gao C (2015) *ACS Nano* 9:5214
215. Zhang E, Wang T, Zhao L, Sun W, Liu X, Tong Z (2014) *ACS Appl Mater Interfaces* 6:22855
216. Wan SJ, Li YC, Peng JS, Hu H, Cheng QF, Jiang L (2015) *ACS Nano* 9:708
217. Ramphal IA, Hagerman ME (2015) *Langmuir* 31:1505
218. Lee YR, Kim IY, Kim TW, Lee JM, Hwang S-J (2012) *Chem Eur J* 18:2263
219. Wan-Guo H, De-Jun S, Shu-Hua H, Chun-Guang Z, Guo-Ting W (1998) *Colloid Polym Sci* 276:274
220. Li SP, Hou WG, Sun DJ, Guo PZ, Jia CX (2003) *Langmuir* 19:3172
221. Werner S, Lau VW, Hug S, Duppel V, Clausen-Schaumann H, Lotsch BV (2013) *Langmuir* 29:9199
222. Hu Q, Xu Z, Qiao S, Haghseresht F, Wilson M, Lu GQ (2007) *J Colloid Interface Sci* 308:191
223. Deák Á, Janovák L, Tallósy SP, Bitó T, Sebők D, Buzás N, Pálíno I, Dékány I (2015) *Langmuir* 31:2019
224. Nakato T, Yamada Y, Nakamura M, Takahashi A (2011) *J Colloid Interface Sci* 354:38
225. Nakato T, Inoue S, Hiraragi Y, Sugawara J, Mouri E, Aritani H (2014) *J Mater Sci* 49:915
226. van Olphen H (1977) *An introduction to clay colloid chemistry*, 2nd edn. Krieger, Malabar
227. Dijkstra M, Hansen JP, Madden PA (1995) *Phys Rev Lett* 75:2236
228. Jönsson B, Labbez C, Cabane B (2008) *Langmuir* 24:11406
229. Tombácz E, Szekeres M (2004) *Appl Clay Sci* 27:75
230. Mongondry P, Tassin JF, Nicolai T (2005) *J Colloid Interface Sci* 283:397
231. Nicolai T, Cocard S (2001) *Eur Phys J E* 5:221
232. Pignon F, Magnin A, Piau J-M (1996) *J Rheol* 40:573
233. Schmidt G, Nakatani AI, Butler PD, Han CC (2002) *Macromolecules* 35:4725
234. Norrish K (1954) *Discuss Faraday Soc* 18:120
235. Mourchid A, Delville A, Levitz P (1995) *Faraday Discuss* 101:275
236. Avery RG, Ramsay JDF (1986) *J Colloid Interf Sci* 109:448
237. Rand B, Peken E, Goodwin JW, Smith RW (1980) *J Chem Soc Faraday Trans 1*(76):225
238. Shalkevich A, Stradner A, Bhat SK, Muller F, Schurtenberger P (2007) *Langmuir* 23:3570
239. Bonn D, Kellay H, Tanaka H, Wegdam G, Meunier J (1999) *Langmuir* 15:7534
240. Abend S, Lagaly G (2000) *Appl Clay Sci* 16:201
241. Penner D, Lagaly G (2001) *Appl Clay Sci* 19:131
242. Permien T, Lagaly G (1994) *Appl Clay Sci* 9:251
243. Levitz P, Lecolier E, Mourchid A, Delville A, Lyonard S (2000) *Europhys Lett* 49:672
244. Kroon M, Wegdam GH, Sprik R (1996) *Phys Rev B* 54:6541
245. Ramsay JDF, Lindner P (1993) *J Chem Soc Faraday Trans* 89:4207
246. Ramsay JDF (1986) *J Colloid Interface Sci* 109:441
247. Ramsay JDF, Swanton SW, Bunce J (1990) *J Chem Soc Faraday Trans* 86:3919
248. Balnois E, Durand-Vidal S, Levitz P (2003) *Langmuir* 19:6633

249. Ruzicka B, Zulian L, Ruocco G (2006) *Langmuir* 22:1106
250. Tanaka H, Meunier J, Bonn D (2004) *Phys Rev E* 69:031404
251. Ruzicka B, Zulian L, Ruocco G (2004) *Phys Rev Lett* 93: 258301
252. Ruzicka B, Zulian L, Angelini R, Sztucki M, Moussaïd A, Ruocco G (2008) *Phys Rev E* 77:020402
253. Ruzicka B, Zulian L, Ruocco G (2004) *J Phys: Condens Matter* 16:S4993
254. Jabbari-Farouji S, Wegdam GH, Bonn D (2007) *Phys Rev Lett* 99:065701
255. Jabbari-Farouji S, Wegdam GH, Bonn D (2008) *Phys Rev E* 78:061405
256. Tanaka H, Jabbari-Farouji S, Meunier J, Bonn D (2005) *Phys Rev E* 71:021402
257. Labanda J, Sabaté J, Llorens J (2007) *Colloids Surf A* 301:8
258. Nakato T, Miyamoto N (2002) *J Mater Chem* 12:1245
259. Nakato T, Miyamoto N, Harada A, Ushiki H (2003) *Langmuir* 19:3157